The Thesis Committee for Olabode Ijasan
Certifies that this is the approved version of the following thesis:

Rapid Modeling of LWD Nuclear Measurements Acquired in High-Angle and Horizontal Wells for Improved Petrophysical and Geometrical Interpretation

APPROVED BY
SUPERVISING COMMITTEE:

Carlos Torres-Verdín, Supervisor

William E. Preeg

Rapid Modeling of LWD Nuclear Measurements Acquired in High-Angle and Horizontal Wells for Improved Petrophysical and Geometrical Interpretation

by

Olabode Ijasan, B.S.

Thesis

Presented to the Faculty of the Graduate School of
The University of Texas at Austin
in Partial Fulfillment
of the Requirements
for the Degree of

Master of Science in Engineering

The University of Texas at Austin
December 2010

Dedication

To my mother, Oseola Akanke

Acknowledgements

I specially thank my supervisor, Dr. Carlos Torres-Verdín, for his guidance and consistent support for the work in this thesis. My sincere gratitude goes to my co-supervisor, Dr. William Preeg, for his advice and contributions to developments in this research.

The work reported in this paper was funded by The University of Texas at Austin’s Research Consortium on Formation Evaluation, jointly sponsored by Anadarko, Aramco, Baker-Hughes, BG, BHP Billiton, BP, Chevron, ConocoPhillips, ENI, ExxonMobil, Halliburton, Hess, Marathon, Mexican Institute for Petroleum, Nexen, Pathfinder, Petrobras, Repsol-YFP, RWE, Schlumberger, Statoil, Total, and Weatherford.

Special thanks to Alberto Mendoza for his mentorship, patience, and help through out this work. My thanks also go to Rey Casanova, Cheryl Kruzie, Frankie Hart, Roger Terzian and Tim Guinn for their administrative and technical support.

My thanks to Ben Voss, Andy Popielski, Jordan Mimoun, Renzo Angeles, Robert Mallan, Zoya Heidari, Jorge Sanchez, Echez Uzoh, Hamid Hadibeik, Chicheng Xu, Vahid Shabro, Rohollar Pour, Tatyana Torskaya, Amir Frooqnia, Phillipe Maoruby, Oyinkan Ajayi, Edwin Ortega, Malek Lemkecher, Ali Monifar, and Amir Reza-Rahmani.

I would like to thank ExxonMobil Upstream Research Company and ExxonMobil Exploration Company for the rewarding internships during the summers of 2009 and 2010 respectively. My gratitude to Duncan Mardon, Russell Spears, and Dale Fitz.

Finally, I would like to thank my family for all their support and encouragement.

December 2010

Abstract

Rapid Modeling of LWD Nuclear Measurements Acquired in High-Angle and Horizontal Wells for Improved Petrophysical and Geometrical Interpretation

Olabode Ijasan, M.S.E.
The University of Texas at Austin, 2010

Supervisor: Carlos Torres-Verdín

Nuclear logging-while-drilling (LWD) measurements acquired in high-angle and horizontal (HA/HZ) wells are influenced by tool, geometrical, and petrophysical effects. Reliable interpretation of petrophysical and geometrical properties from LWD measurements acquired in thinly-bedded formations requires that gamma ray, density, photoelectric (PEF), and neutron measurements be quantitatively integrated with explicit consideration of their effective volume of investigation (EVOI). One of the effects of different tool EVOIs is false gas density-neutron crossovers across thinly-bedded formations. Also, in the presence of tool eccentricity, azimuthally-varying standoff gives rise to an azimuthally-varying effective depth of investigation (EDOI), which introduces errors in the inference of formation dip.

Conventional Monte Carlo simulations of nuclear measurements are computationally expensive in reproducing multi-sector LWD responses in HA/HZ wells. Using linear iterative refinement of pre-calculated flux sensitivity functions (FSFs), we introduce a fast method for numerical simulation of LWD nuclear images in the presence of tool eccentricity along any well trajectory.

Our investigation of measurement responses from FSFs motivates techniques to explicitly consider the EVOI of LWD nuclear measurements. Simple radial DOI and standoff corrections suffice for interpretation of gamma-gamma images but are inadequate for neutron responses due to larger EVOI and azimuthal aperture. We introduce a new azimuthal deconvolution method of neutron images to improve bed-boundary detection. Neutron DOI varies significantly with porosity, whereby we correct neutron images for penetration length due to changes of porosity along the well trajectory. In addition, we implement a new method of separate linear iterative refinement on neutron thermal group responses to improve the resolution of neutron images across heterogeneous and thinly-bedded formations. The method reduces shoulder-bed effects and false neutron-density gas crossovers. We corroborate these techniques with rigorous Monte Carlo simulations in vertical and deviated wells.

A field example of application conclusively indicates that numerical simulation of LWD nuclear measurements is necessary for reliable estimation of petrophysical properties.

Table of Contents

List of Tables

List of Figures

Chapter 1: Introduction

As more HA/HZ wells are drilled in the world, LWD measurement and interpretation are rapidly becoming the primary method of formation evaluation. This emphasizes the need for fast and accurate simulation of multi-sector LWD nuclear responses in HA/HZ wells. A better understanding of geometrical and petrophysical effects can be achieved with forward modeling, for improved environmental and geometrical corrections and for increased confidence in predicted formation properties. Extensive technical literature exists on improved processing techniques of LWD density measurements (e.g. enhanced alpha-processing, Flaum et al., 1987; Galford et al., 1986) for image-derived bulk density with relatively scant attention to azimuthal neutron and natural gamma ray measurements. Integrated nuclear modeling requires improvements in data processing techniques for neutron and gamma ray measurements.

1.1 BACKGROUND

Uzoh et al. (2009) investigated the influence of bed thickness and relative dip on LWD density and PEF images using Monte Carlo simulations with a 16-sector azimuthal binning scheme. The study included back-calculating effective penetration lengths (EPL) from short-spaced, long-spaced, and compensated density measurements. Guo et al. (2008) defined the “Gamma Borehole Diameter” as the borehole diameter plus two times EDOI of the density tool. This parameter is used to accurately calculate relative bed dip. Yin et al. (2006) studied thin-bed, dip, borehole shape and EDOI effects on LWD neutron and density measurements in vertical and deviated wells when the tool was centered in the borehole. They quantified dip estimation errors from detector measurements while illustrating the corresponding effects on true stratigraphic thickness (TST) estimation. Yin et al. (2008) parameterized EVOI as a function of radial DOI, axial resolution, and azimuthal aperture for an LWD dual-detector density tool. They also introduced a method of image processing with azimuth-dependent depth shifts. The method improved estimation of bed boundaries and dip from density images obtained with a borehole centered tool. Mendoza et al. (2007, 2010a and 2010b) illustrated the use of linear iterative refinement on MCNP pre-calculated spatial FSFs for rapid simulation of nuclear measurements in heterogeneous and complex formations. Heidari et al. (2009) showed that this technique was accurate and efficient for interactive fast-forward modeling of wireline nuclear measurements in vertical and deviated wells.

1.2 OBJECTIVES

In this thesis, we develop new processing and modeling techniques to reduce false gas crossovers across thinly-bedded formations and improve formation dip and porosity estimation in HA/HZ wells. To that end, we characterize LWD nuclear responses (neutron-neutron, gamma-gamma and natural gamma ray) for EVOI across varying formation properties using generic tool models. We appropriately adapt traditional correction techniques by considering the disparities in EVOI in the three nuclear responses. Also, we implement the FSF fast-forward technique to simulate multi-sector LWD measurements. Further, we study the effect of tool eccentricity on borehole image amplitude, quantify the consequent error in relative dip estimation, and adapt EPL corrections for tool eccentricity.

Finally, we apply the above techniques to field measurements acquired in a HA/HZ well for combined quantitative assessment of petrophysical and geometrical effects of LWD neutron-neutron, gamma-gamma, and natural gamma ray measurements.

1.3 OUTLINE OF THE THESIS

Following the introductory chapter, the thesis consists of five additional chapters. Chapter 2 gives descriptions and governing measurement physics of generic LWD nuclear tool models used in this thesis. Chapter 3 parameterizes tool response sensitivities in formations with varying properties. Using numerical simulations, Chapter 4 introduces new concepts in nuclear image processing. In Chapter 5, we apply the discussed simulation and modeling concepts to a field case. Chapter 6 gives the summary, conclusions, and recommendations stemming from the thesis.

Chapter 2: Longhorn LWD Nuclear Tools

In this chapter, I provide detailed descriptions of generic LWD nuclear tool models used in the thesis. Generic LWD tool models, comprising tool components, borehole, and formation, were developed in conjunction with the Monte Carlo N-Particle (MCNP) code developed by the Los Alamos National Laboratory (X-5 Monte Carlo Team, 2005). Results from MCNP simulations include detector count rates and spatial three-dimensional FSFs. I refer to these generic models as the "Longhorn LWD Nuclear Tools". Tool models were developed assuming an 8.5-inch steel collar. All calculations were performed under the assumption of fresh water-filled boreholes while neglecting mudcake buildup.

2.1 LONGHORN LWD GAMMA-GAMMA TOOL

The Longhorn LWD gamma-gamma or density tool (LLDT) consists of two sodium iodide (NaI) scintillation detectors and a 1.7-curie Caesium-137 (^{137}Cs) source emitting low energy gamma rays at 662 keV. **Table 2.1** summarizes the geometrical properties of the LLDT shown in **Figure 2.1**. Gamma ray interactions of particular study in well logging are Compton scattering and photoelectric absorption (Ellis et al., 2007). Compton scattering has a direct relationship to the electron density, ρ_e of the formation and its physics is the primary mode for bulk density, ρ_b measurement. Electron density is given by

$$\rho_e = 2\frac{Z}{A_r}\rho_b \ , \tag{2.1}$$

where Z and A_r are the atomic number and atomic weight, respectively. Photoelectric absorption is influenced by the atomic number of the formation and it dominates gamma ray interactions at energies below 100 keV for most lithologies. The photoelectric factor (PEF), with units of barns per electron [b/e], is approximated by

$$PEF = \left(\frac{Z}{10}\right)^{3.6} . \tag{2.2}$$

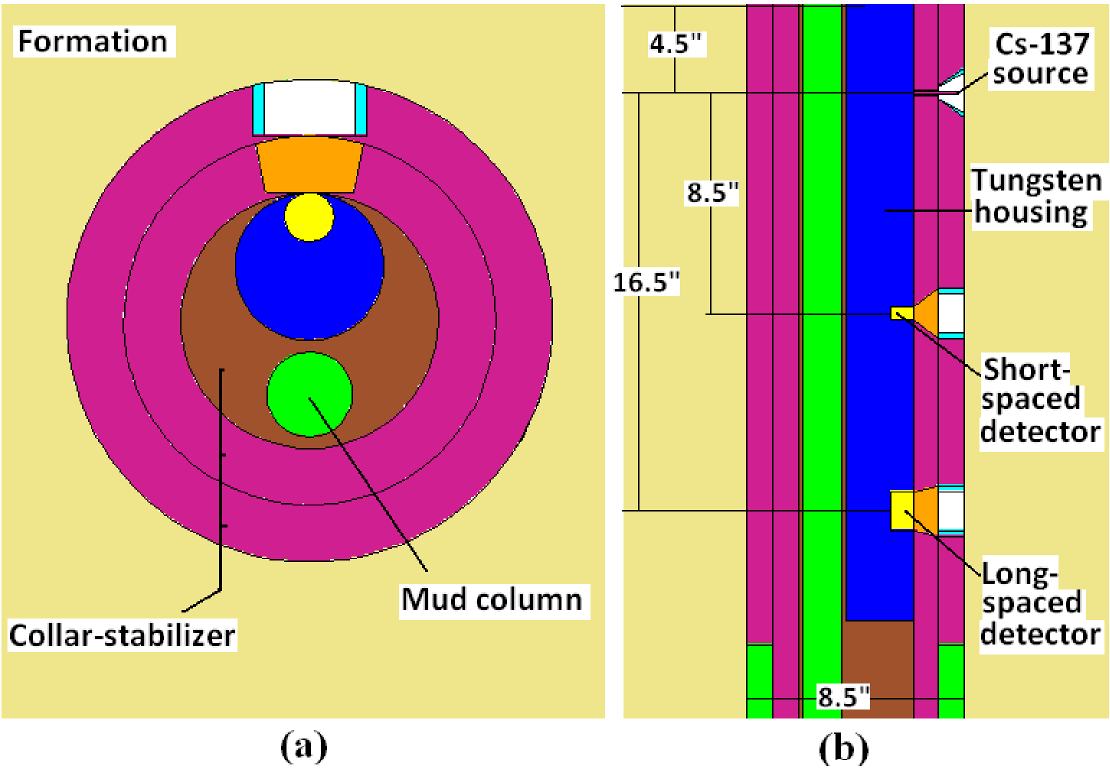

Figure 2.1: **(a)** Top cross-sectional view of the LLDT showing collar-stabilizer assembly (red and brown). **(b)** Side cross-sectional view of the LLDT. Detector spacing dimensions are measured from the source location and are described in inches.

Variable	**Value**	**Units**
Housing length	25.5	inches
Housing diameter	2.6	inches
Collar-stabilizer diameter	8.5	inches
Drill-pipe diameter	1.5	inches
Short-spaced detector distance	8.5	inches
Short-spaced detector diameter	0.8	inches
Short-spaced detector length	0.5	inches
Long-spaced detector distance	16.5	inches
Long -spaced detector diameter	0.8	inches
Long -spaced detector length	1.5	inches
^{137}Cs source location from top of housing	4.5	inches

Table 2.1: Geometrical properties of the Longhorn LWD density tool (LLDT). Detector distances are measured from the source location.

2.2 LONGHORN LWD NEUTRON-NEUTRON TOOL

The Longhorn LWD neutron-neutron tool (LLNT) consists of a 14 MeV D-T (deuterium-tritium) neutron generator with a source strength of 10^8 neutrons per second and two Helium (^{3}He) detectors. **Table 2.2** summarizes the geometrical properties of the LLNT, shown in **Figure 2.2**. Neutron interactions and porosity measurements acquired with the LLNT are directly related to the hydrogen index (HI) of the bulk formation. Neutrons in the thermal energy range (below 0.41eV) are primarily transported by diffusion before their final capture. The root-mean-square distance traveled in this energy range is referred to as the diffusion length, L_d and is given by

$$L_d = \sqrt{D_{coeff} / \Sigma_a} \,, \tag{2.3a}$$

where D_{coeff} is thermal diffusion coefficient and Σ_a is macroscopic thermal absorption cross section of the bulk formation. Migration length, L_m, is viewed as the combined path traveled during slowing down, L_s and diffusion, L_d and is approximated by

$$L_m^2 = L_s^2 + L_d^2 \,. \tag{2.3b}$$

To transform measurements to porosity values we use near-to-far counts ratio versus porosity for calibration. Ellis et al. (2007) showed that a linear relationship occurs between near-to-far ratio and inverse of migration (L_m) and slowing-down (L_s) lengths because of their dependence on the macroscopic energy cross section (Σ). This property makes the inverse of the characteristic lengths an important and useful weighting parameter in sensitivity calculations.

Variable	**Value**	**Units**
Collar diameter	8.5	inches
Drill-pipe diameter	3	inches
Far detector distance	24	inches
Far detector diameter	2.25	inches
Far detector length	8	inches
Near detector distance	15	inches
Near detector diameter	2	inches
Near detector length	5	inches

Table 2.2: Geometrical descriptions of the Longhorn LWD neutron-neutron tool (LLNT). Distances are measured from source location.

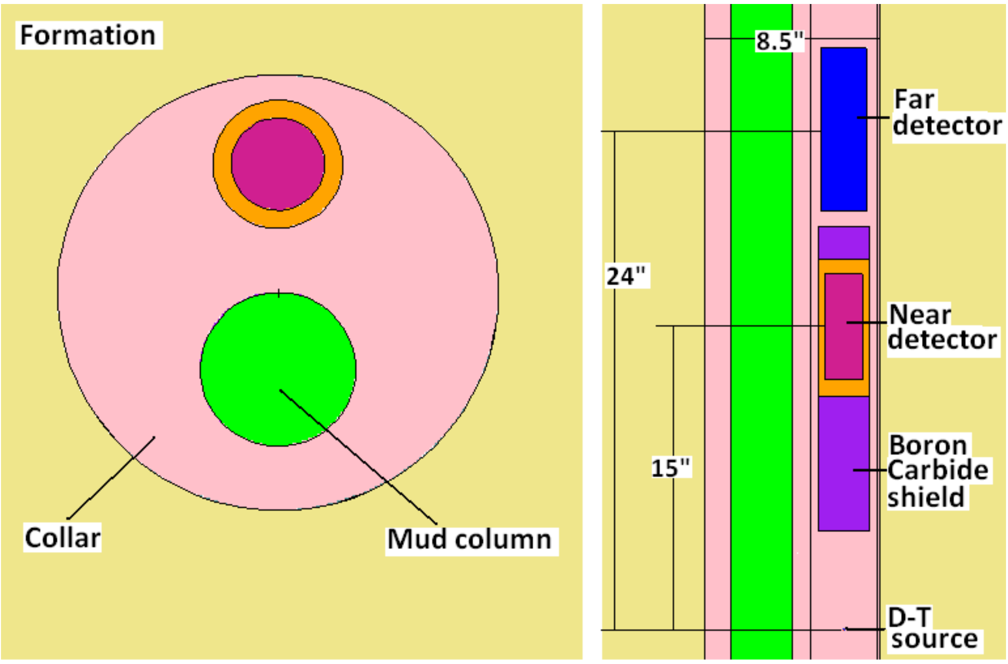

(a) (b)

Figure 2.2: **(a)** Top cross-sectional view of the LLNT. **(b)** Side cross-sectional view of the LLNT. Detector spacing dimensions are measured from the source location and are described in inches.

2.3 LONGHORN LWD GAMMA RAY TOOL

The LWD gamma ray tool (LLGT) consists of a single sodium iodide (NaI) detector. The tool measures gamma ray activity caused by naturally occurring potassium (^{40}K), thorium (^{232}Th) and uranium (^{238}U) isotopes in rock formations. Pulse height spectrum (S_i) is simulated for each isotope (Mendoza et al., 2006). Gamma ray response in API units is calculated using

$$GR_{API} = -0.693 N_{av} f \sum_{i}^{U,Th,K} \left\{ \frac{\rho_i}{M_i T_{1/2,i}} \int dS_i \right\} m_i \, , \tag{2.4}$$

or, more concisely,

$$GR_{API} = A_{api} \cdot U_{ppm} + B_{api} \cdot Th_{ppm} + C_{api} \cdot K_{\%}\,, \tag{2.5}$$

where the calibration coefficients A_{api}, B_{api}, and C_{api}, for each isotope is obtained with

$$G_i = -0.693 N_{av} f \frac{\rho_i}{M_i T_{1/2,i}} \int dS_i\,, \tag{2.6}$$

The quantity G_i above is a calibration coefficient calculated from the respective isotope pulse spectrum, ρ_i is density of the isotope, M_i is the molecular weight of the isotope, $T_{½,i}$ is the half-life of the isotope, m_i is the mass concentration of the isotope, N_{av} is Avogadro's number, and f is calibration factor.

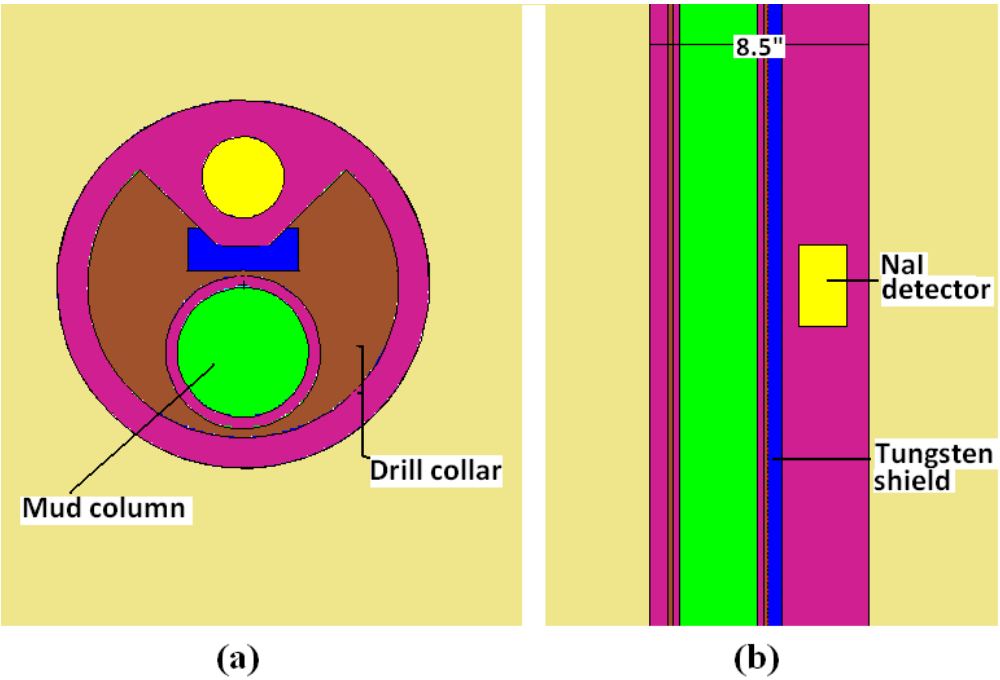

Figure 2.3: **(a)** Top cross-sectional view of the LLGT. **(b)** Side cross-sectional view of the LLGT.

Variable	Value	Units
NaI detector length	3.5	inches
NaI detector diameter	1.75	inches
Drill-pipe diameter	3	inches
Drill collar diameter	8.5	inches
Coefficient A_{api}	6.23	-
Coefficient B_{api}	2.57	-
Coefficient C_{api}	15.90	-

Table 2.3: Geometrical descriptions and calibration coefficients of the Longhorn LWD gamma ray tool (LLGT).

2.4 AZIMUTHAL MEASUREMENTS IN THE PRESENCE TOOL ECCENTRICITY

We implement an 8-sector binning scheme for the acquisition of natural gamma-ray measurements and a 16-sector binning scheme for density and neutron measurements, including sensitivity calculations. In the presence of tool eccentricity, gravity pulls the tool to the bottom of the borehole causing zero tool standoff in the bottom sector and maximum tool standoff in the top sector. Therefore, as the tool rotates the highest quality measurements are obtained in the bottom quadrant (Radke et al., 2003) and we observe a substantial variation of spatial flux sensitivities with azimuth. These variations suggest that EVOI changes as the tool rotates in the borehole. **Figure 2.4** shows radial and azimuthal spatial discretization of the Longhorn models for numerical sensitivity calculations when the tool is fully eccentered.

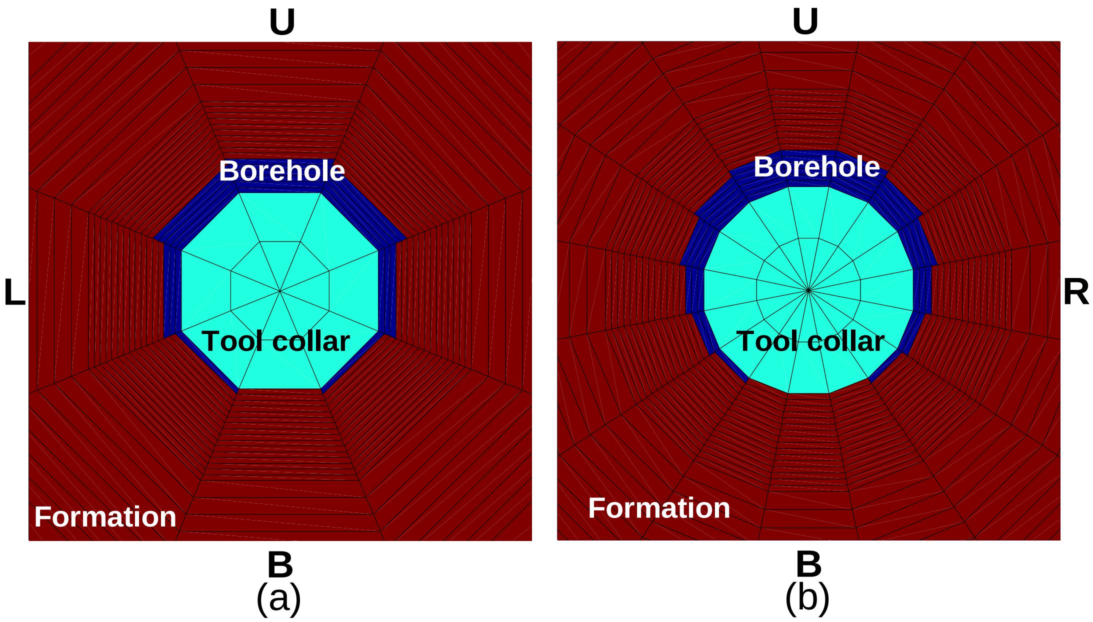

Figure 2.4: **(a)** Radial and azimuthal spatial discretization of a fully eccentered tool for numerical sensitivity calculations and tool orientation using an 8-sector binning scheme. The bottom (B), upper (U), left (L), and right (R) sectors are indicated for reference. **(b)** Similar to (a) but for a 16-sector binning scheme.

Chapter 3: LWD Nuclear Response Characteristics

In this chapter, I describe EVOI in terms of three parameters: effective radial DOI, axial resolution, and azimuthal aperture (Yin et al., 2008). In vertical wells, assuming horizontal beds (i.e. zero relative dip), radial DOI affects bed measurement values whereas axial resolution influences bed boundary detection with azimuthal aperture having the least effect on measurements. As relative dip or well deviation increases, the three parameters equally influence bed measurement values and boundary detection. This behavior requires proper definition of EVOI collectively in terms of the geometrical parameters involved in HA/HZ wells.

3.1 EFFECTIVE VOLUME OF INVESTIGATION, EVOI

Spatial FSFs are numerical adjoint solutions to the particle transport problem; their one-dimensional descriptions are the basis for EVOI parameterization, namely,

$$EVOI = \Delta D^2 \cdot AR \cdot \Delta\psi \text{ (Yin et al., 2008),} \tag{3.1}$$

where ΔD is the effective radial DOI into the formation, AR is axial resolution, and $\Delta\psi$ is the tool's azimuthal aperture. ΔD is calculated from the 90% contribution of the radial J-factor. AR is obtained by integrating the FSF in the radial and azimuthal directions and calculating the 80% resolution about the response's geometric mean. Similarly, $\Delta\psi$ is the angular ratio of 80% azimuthal resolution of the FSF integrated in the axial and radial directions. **Figures 3.1-3.4** show 1-D FSF profiles for the generic LWD tools.

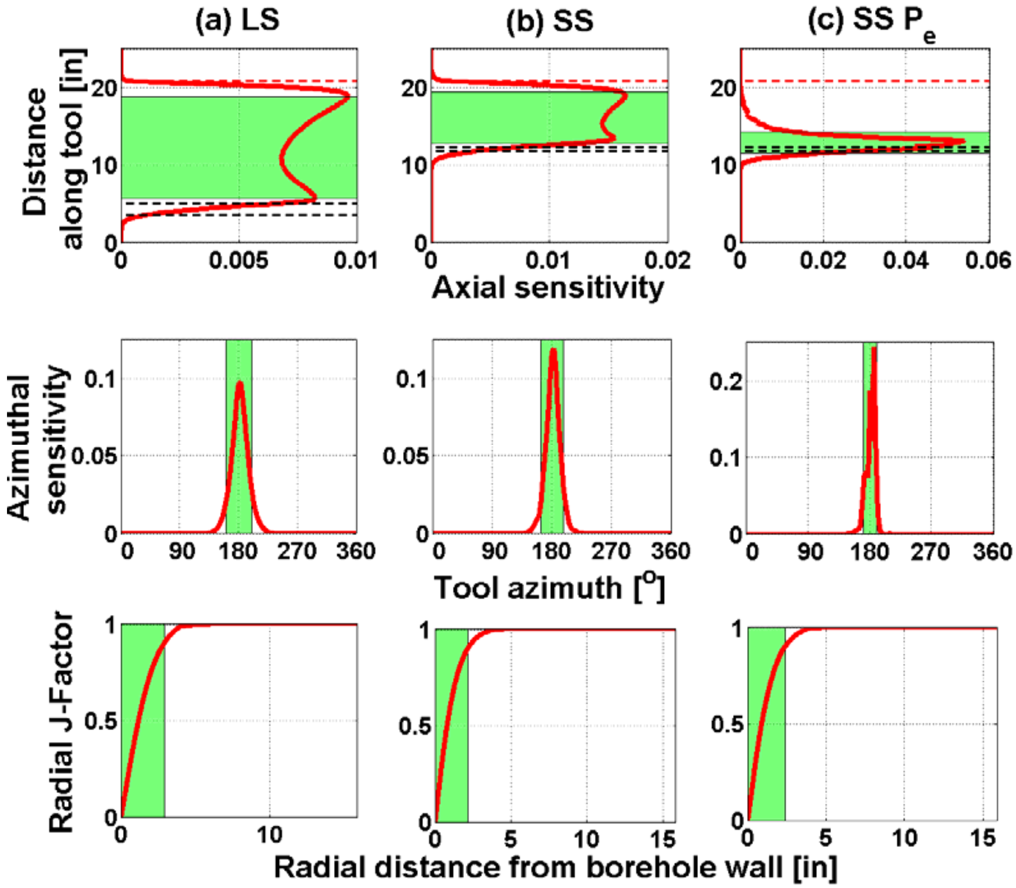

Figure 3.1: Spatial 1D radial FSF response of the LLDT in a 2.32 g/cc formation. **(a)** Long-spaced detector response. The top panel describes axial sensitivity along the tool (solid red curve) with *AR* shaded in green. Red dashed line indicates source location and black dashed lines indicate detector location. The middle panel shows azimuthal sensitivity with $\Delta\psi$ shaded in green. The bottom panel shows the radial J-factor with ΔD shaded in green**.** **(b)** Similar to (a) but for short-spaced detector. **(c)** Similar to (a) but for short-spaced detector PEF response.

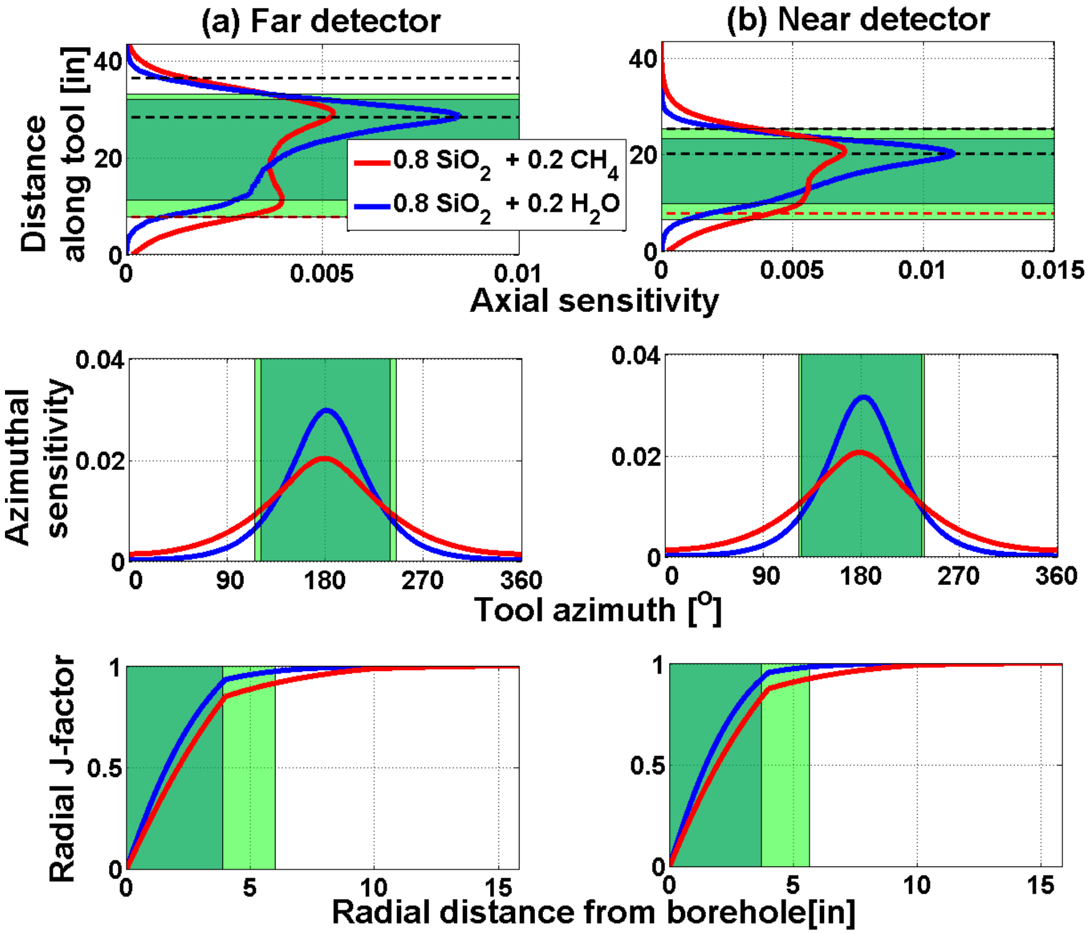

Figure 3.2: Spatial 1D total/fast neutron FSF response of the LLNT in a 20 p.u. water- and methane-filled sandstone formation. **(a)** Far detector response. The top panel shows axial sensitivity along the tool in a 20 p.u. water-filled formation (solid blue curve) and a 20 p.u. methane-filled formation (solid red curve). AR is shown in light green for a methane-filled formation and dark green for a water-filled formation. Red dashed line indicates source location and black dashed lines indicate detector location. The middle panel shows azimuthal sensitivity with $\Delta\psi$ shaded in light green for a methane-filled formation and dark green for a water-filled formation. The bottom panel shows the radial J-factor with ΔD shaded in dark green for a water-filled formation and light green for a methane-filled formation. **(b)** Similar to (a) but for near detector response.

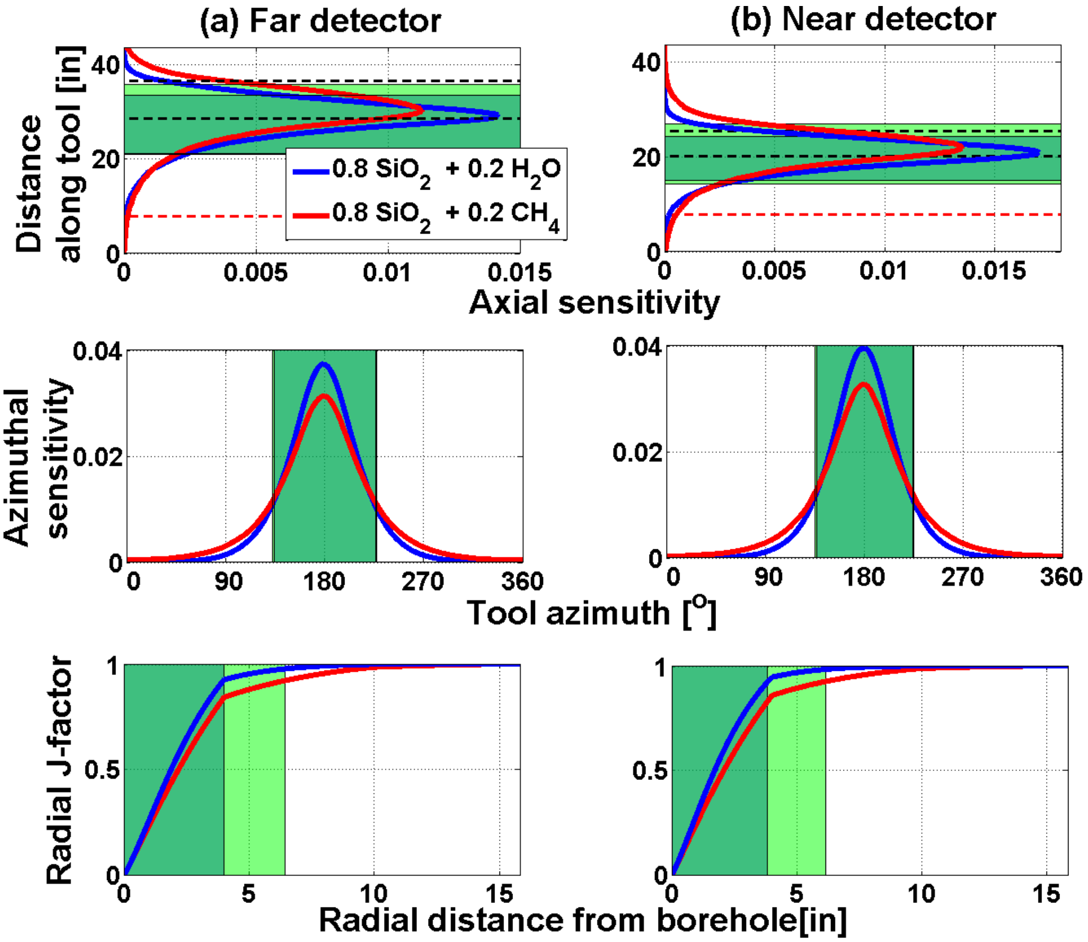

Figure 3.3: Spatial 1D radial thermal/slow neutron FSF response of the LLNT in a 20 p.u. water- and methane-filled sandstone formation. **(a)** Far detector response. The top panel shows axial sensitivity along the tool in a 20 p.u. water-filled formation (solid blue curve) and a 20 p.u. methane-filled formation (solid red curve). *AR* is shown in light green for methane-filled formation and dark green for water-filled formation. Red dashed line indicates source location and black dashed lines indicate detector location. The middle panel shows azimuthal sensitivity with $\Delta\psi$ shaded in light green for a methane-filled formation and dark green for a water-filled formation. The bottom panel shows the radial J-factor with ΔD shaded in dark green for a water-filled formation and light green for a methane-filled formation. **(b)** Similar to (a) but for near detector response.

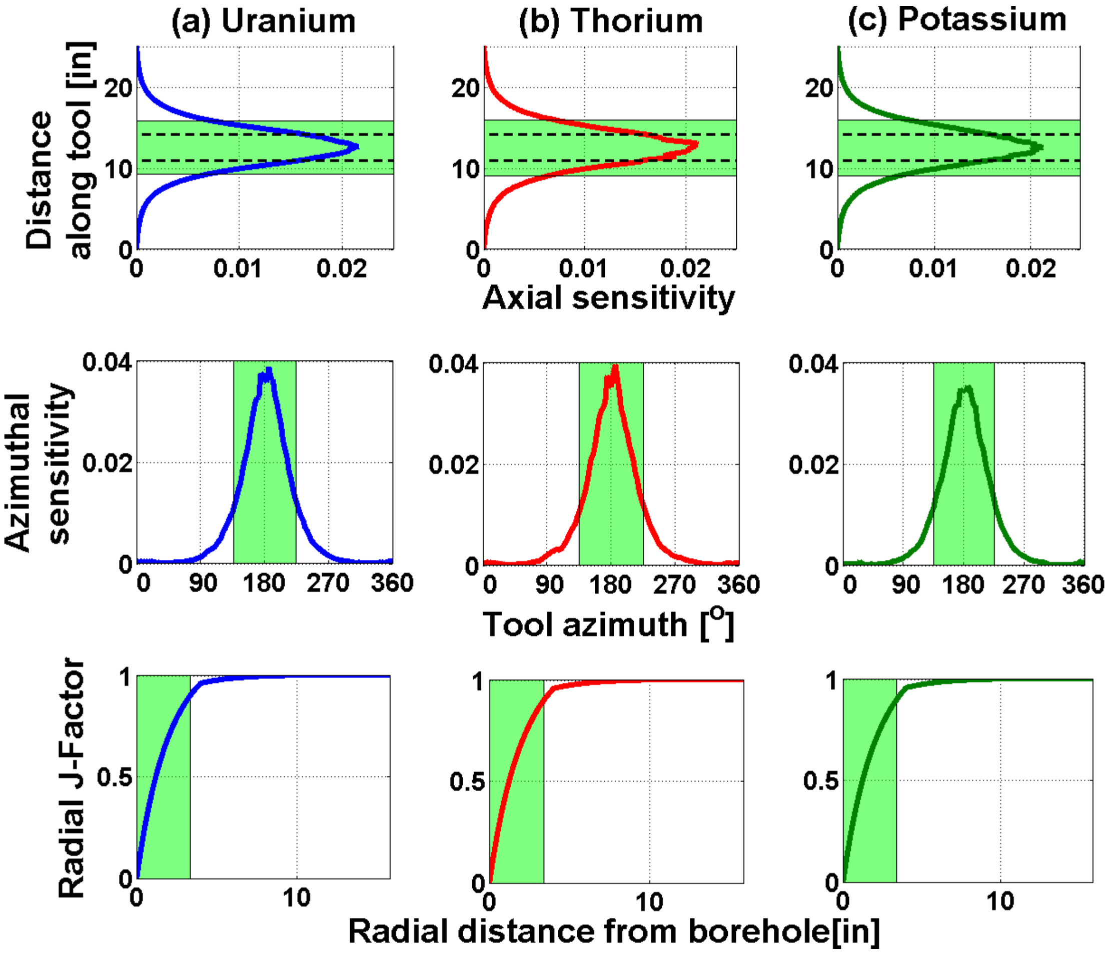

Figure 3.4: Spatial 1D radial FSF response of the LLGT in a 2.41 g/cc kaolinite formation. **(a)** Uranium response of the gamma ray tool. The top panel shows the axial sensitivity along the tool. Black dashed lines indicate detector location. ΔR is shaded in green. The middle panel indicates azimuthal sensitivity with $\Delta\psi$ shaded in green. The bottom panel shows the radial J-factor with ΔD shaded in green. **(b)** Similar to (a) but for thorium isotope. **(c)** Similar to (a) but for potassium isotope.

3.2 PETROPHYSICAL AND GEOMETRICAL EFFECTS OF DIFFERING RESPONSE CHARACTERISTICS

Figure 3.5 shows plots of EVOI calculated from equation 3.1 in various formation base cases for density, neutron, and gamma ray tools in an 8.5” borehole. The plots show significant differences in EVOI for different nuclear measurements. We observe that the gamma ray tool exhibits fairly constant EVOIs irrespective of the radioactive isotope. Similarly, the density tool has relatively constant parameters irrespective of formation density. The neutron tool exhibits the largest EVOIs and widest variations in response parameters with respect to migration length. Formation base cases and calibration plots of the Longhorn LWD tools are summarized in Appendix A.

In **Figures 3.1** and **3.2**, $\Delta\psi$ of the density tool is approximately 20^o while the neutron is approximately 120^o. The effect of this disparity is inconsistent dip estimation from density and neutron measurements, especially at bed boundaries in HA/HZ wells where formation heterogeneity is pronounced. **Figure 3.3** shows response radial profiles for thermal neutrons detected with the LLNT. An important observation is that thermal neutron AR is approximately equal to the density tool’s AR. It is this property of the thermal FSF that we use to improve vertical resolution in neutron porosity simulations.

In the presence of tool eccentricity, ΔD shortens in the top azimuth, thereby causing an azimuthally dependent EVOI**.** This behavior in turn compounds the uncertainties in petrophysical interpretation and relative dip estimation from nuclear images.

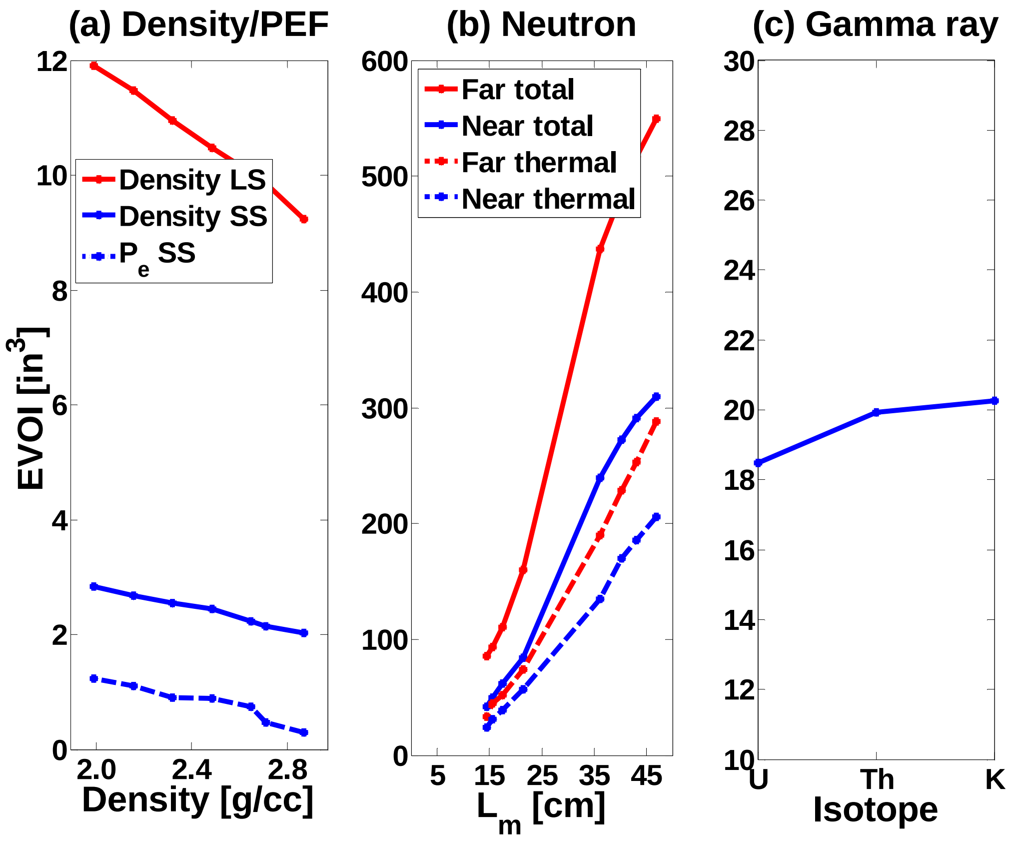

Figure 3.5: EVOI, in inches^3, calculated from equation 3.1. **(a)** Density and PEF EVOIs versus formation density. Solid red curve indicates long-spaced detector EVOI, solid blue curve indicates short-spaced detector EVOI, and dashed blue curve indicates short-spaced P_e EVOI. **(b)** Similar to (a) but for neutron responses. **(c)** Similar to (a) but for gamma ray tool uranium, thorium, and potassium responses.

Chapter 4: Numerical Simulation of LWD Nuclear Measurements

In this chapter, I demonstrate tool eccentricity effect and adapt dip estimation methods of density images to correct for tool eccentricity. Neutron images exhibit the widest $\Delta\psi$ and hence conventional image processing does not suffice. I introduce a new method of neutron azimuthal deconvolution based on one-dimensional azimuthal sensitivity to improve bed boundary detection from neutron images. Also I show how thermal neutrons improve bed measurement resolution across thin beds.

MCNP simulation of multi-sector measurements is computationally expensive and inefficient. I implement the technique of rapid numerical simulation with pre-calculated FSFs (Mendoza et al., 2007; 2010a and b) for LWD measurements. In highly deviated wells, high degree of heterogeneity necessitates adaptive linear iterative refinement, especially in neutron measurements where sensitivity profiles vary widely with HI or L_m.

4.1 TOOL ECCENTRICITY EFFECT

It is usual practice to calculate formation dip from borehole density images. Guo et al. (2008) and Yin et al. (2006) studied dip estimation techniques and EDOI effects on LWD density images for the case of a centered tool. An azimuth-dependent Δh-depth shift correction is applied to the measured depth to accurately predict relative dip and formation density from detector images, i.e.,

$$\Delta h = \Delta D \cdot \cos\alpha \cdot \tan\theta, \tag{4.1}$$

and

$$\theta = tan^{-1}\left[\frac{A-B}{D+2\Delta D}\right], \tag{4.2}$$

where α is image azimuth, θ is true relative dip between borehole and formation bed assuming a zero-degree bed strike, A is location of image crest at the bed boundary, B is location of the image trough at the bed boundary, and D is either tool collar size or borehole size assuming minimum standoff/washouts for a centered tool.

Presence of tool eccentricity skews the borehole image and requires specific geometrical corrections when performing dip estimation and Δh-depth shift calculations from equations 4.1 and 4.2. These corrections account for tool eccentricity effects and are given by

$$\Delta h' = [\Delta D(\phi) - SO_{\alpha}]\cdot cos\ \alpha \cdot\ tan\ \theta \tag{4.3}$$

and

$$\theta' = tan^{-1}\left[\frac{A-B}{D+2\Delta D-SO_{max}}\right], \tag{4.4}$$

where $\Delta D(\phi)$ is DOI varying with porosity. $\Delta D(\phi)$ is approximately constant for density and gamma ray measurements but varies significantly for neutron measurements. SO_{α} is azimuth-dependent standoff and θ' is corrected relative dip. Hence EDOI is equal to $\Delta D(\phi)$ - SO_{α}, which varies with formation and azimuth in the presence of tool eccentricity. Compared to a centered tool, EDOI is equal to ΔD. The “Gamma Borehole Diameter” for a centered tool $D + 2\Delta D$ becomes $D + 2\Delta D - SO_{max}$ for an eccentered tool. It is worth noting that after $\Delta h'$-depth shift corrections, true relative dip θ' becomes

$$\theta' = \tan^{-1}\left[\frac{A'-B'}{D'}\right], \tag{4.5}$$

where *A'* is location of the corrected image crest at the bed boundary, *B'* is location of the corrected image trough at the bed boundary, and *D'* is borehole size. **Figures 4.1 (a)** and **(b)** show a schematic representation of a centered and an eccentered tool, respectively.

A simple synthetic case is numerically simulated with MCNP to illustrate tool eccentricity effects in LWD density images. The formation (**Table 4.1**) has alternating low and high density 1.5ft-thick layers penetrated by an 80° well in a 10" borehole. Simulations are performed with a sampling rate of 0.5 ft measured depth. **Figures 4.2-4.4** show LLDT MCNP simulation results for the synthetic cases obtained with a LLDT 16-sector binning scheme and 2160 hrs of CPU time on a Linux workstation with dual Xeon 3 GHz processors. Mismatch "horns" are observed at bed boundaries in the density logs shown in **Figure 4.2**, which are primarily due to differences in radial DOI between short- and long-spaced detector responses. This effect is pronounced in HA/HZ wells and diminishes as well deviation tends toward the vertical. **Figure 4.3** shows MCNP Δh-corrected images obtained with equation 4.1, i.e. assuming constant EPL and no tool eccentricity. **Figure 4.4** shows the corresponding results with tool eccentricity $\Delta h'$-corrections (equation 4.3). **Table 4.2** summarizes the back-calculated relative dip estimates using equation 4.5. Δh-depth shifts calculated without consideration of tool eccentricity over correct and reduce the image amplitude. For the synthetic case, we observe a 3° error in relative dip estimation.

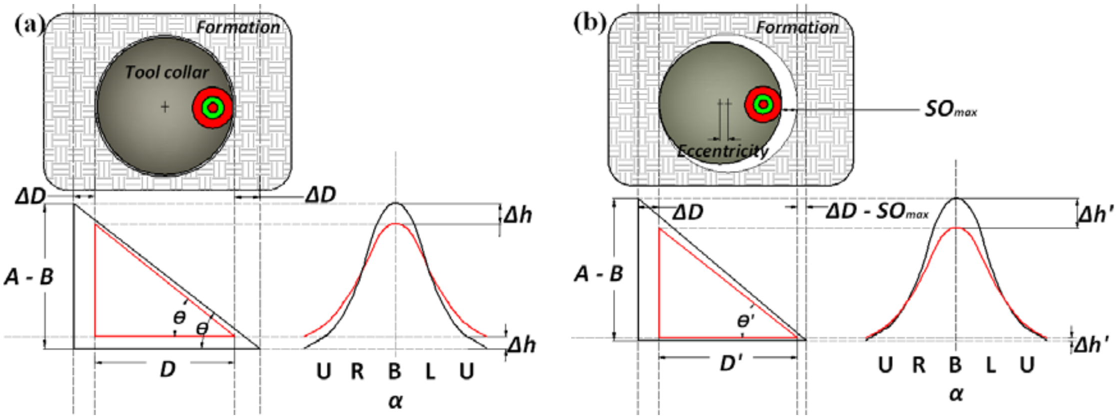

Figure 4.1: Schematic representation of the EDOI/EPL effect on LWD nuclear images for **(a)** a borehole-centered tool with no standoff, and **(b)** a borehole-eccentered tool with maximum standoff, SO_{max} at the top/upper azimuth. Upper (U), right (R), left (L), and bottom (B) azimuths are shown for reference.

Volumetric concentrations

Layer	SiO_2	Kaolinite	$CaCO_3$	ϕ	S_w
I	0.53	0.10	0.10	0.27	0.9
II	0.45	0.10	0.40	0.05	1.0

Properties

Layer	Density [g/cc]	P_e [b/e]	L_m [cm]
I	2.1796	1.98	15.25
II	2.5675	3.12	21.03

Table 4.1: Summary of petrophysical and physical properties for the simple synthetic model.

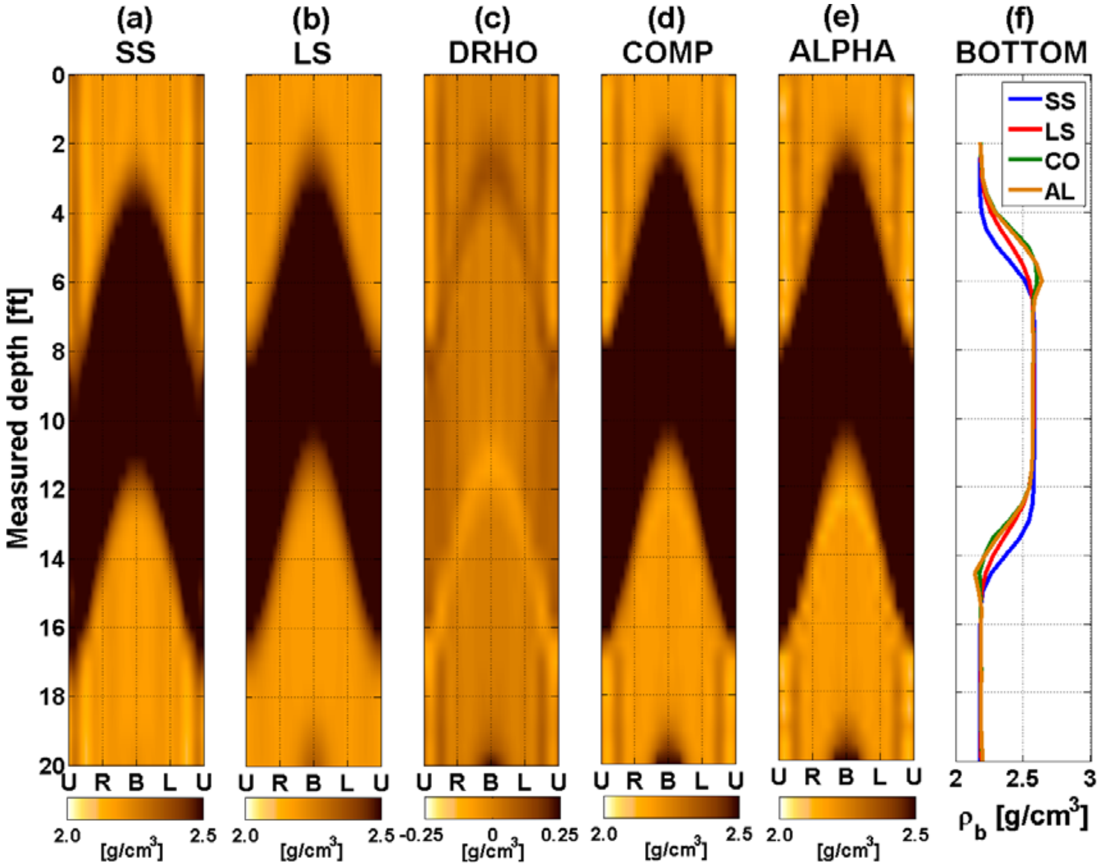

Figure 4.2: Standoff-corrected LLDT MCNP simulation images. **(a)** Density short-spaced image across formation layers in Table 4.1. Light brown represents low density layer I while dark brown represents high density layer II. **(b)** Same as (a) but for long-spaced detector. **(c)** Density correction ($\Delta\rho$) image. **(d)** Same as (a) but for compensated density. **(e)** Same as (a) but for alpha-processed density. **(f)** Bottom quadrant density logs for short-spaced (blue), long-spaced (red), compensated (green), and alpha-processed density (brown).

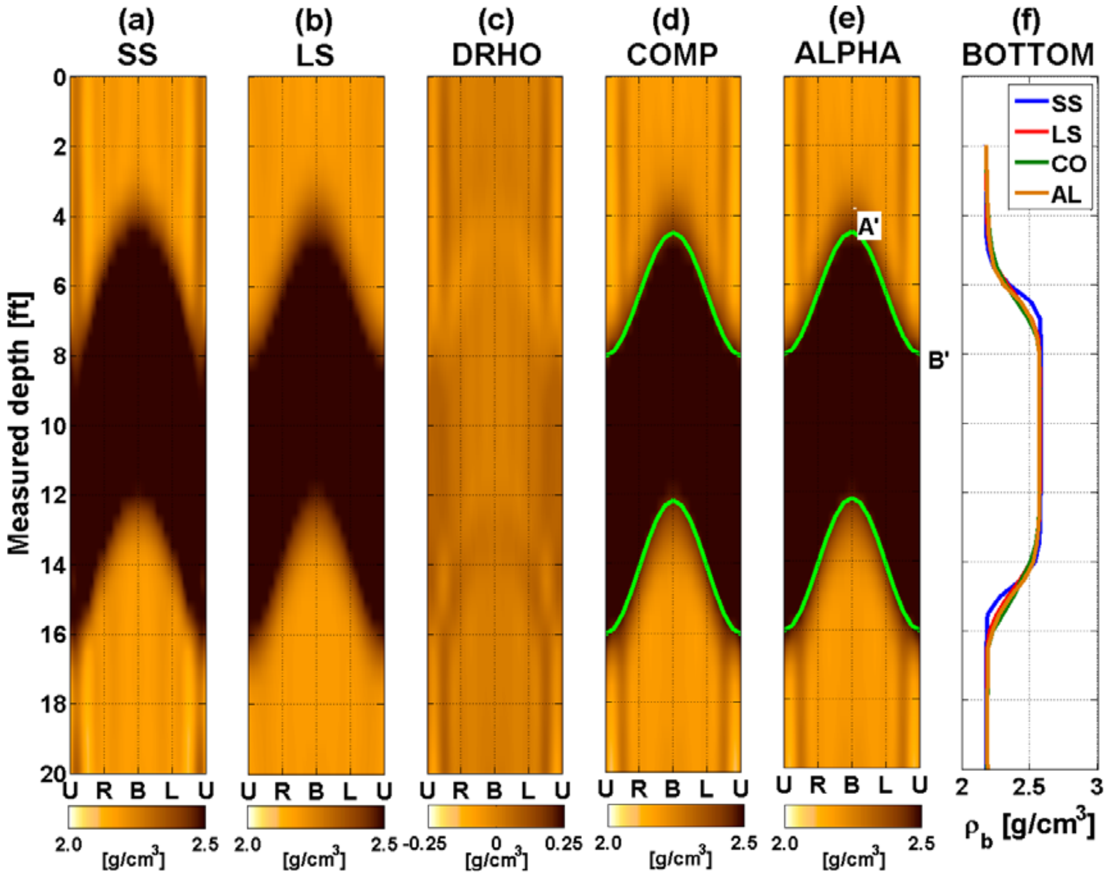

Figure 4.3: *Δh*-corrected (equations 4.1 and 4.2) LLDT MCNP simulation images. **(a)** Density short-spaced image across formation layers described in Table 4.1. Light brown represents low density layer I while dark brown represents high density layer II. **(b)** Same as (a) but for long-spaced detector. **(c)** Density correction (*Δρ*) image. **(d)** Same as (a) but for compensated density. **(e)** Same as (a) but for alpha-processed density. **(f)** Bottom quadrant density logs for short-spaced (blue), long-spaced (red), compensated (green), and alpha-processed density (brown).

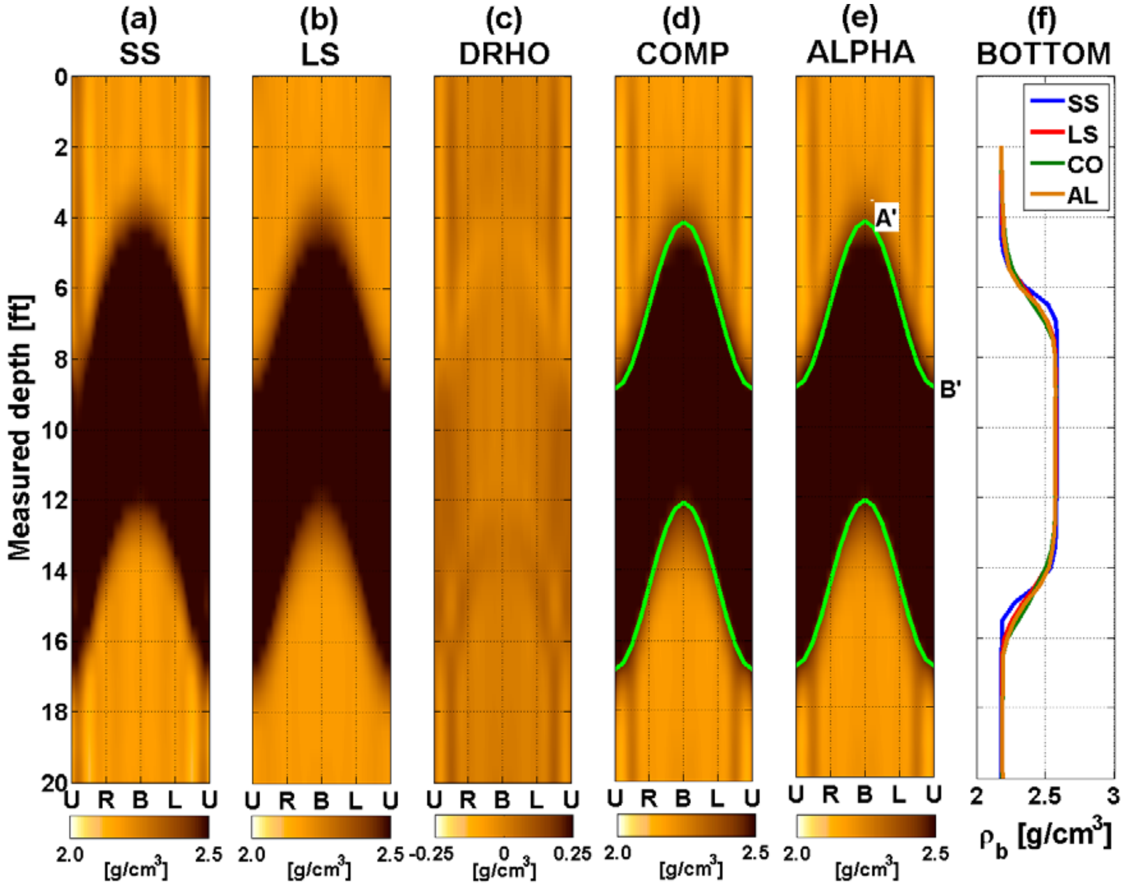

Figure 4.4: *Δh'*-corrected (equations 4.3 and 4.4) LLDT MCNP simulation images. **(a)** Density short-spaced image across formation layers described in Table 4.1. Light brown represents low density layer I while dark brown represents high density layer II. **(b)** Same as (a) but for long-spaced detector. **(c)** Density correction (*Δρ*) image. **(d)** Same as (a) but alpha-processed density. **(f)** Bottom quadrant averaged density log for short-spaced (blue), long-spaced (red), compensated (green), and alpha-processed density (brown).

Method	*A' [ft]*	*B' [ft]*	*A' - B' [ft]*	*D' [in]*	*θ' [^{o}]*
Δh-depth shift corrections	8	4.5	3.5	10	76.6
Δh'-depth shift with tool eccentricity corrections	9	4.5	4.5	10	79.5

Table 4.2: Summary of formation dips back-calculated from corrected density images in an 80^o well.

4.2 NEUTRON AZIMUTHAL DECONVOLUTION

As shown in **Figures 3.2** and **3.3**, the value $\Delta\psi$ for the LLNT is approximately 120^o. Consequently, sector bin measurements are highly influenced by relative dip and adjacent azimuth formation properties. This behavior implies that radial DOI or Δh-depth shift corrections are not sufficient for neutron processing in HA/HZ wells. Our understanding of the LLNT response characteristics from the corresponding FSFs motivates the method of azimuthal deconvolution of neutron detector count rates. If CPS_{ij} is the raw sector bin measurement given in counts per second, at the i-th depth sample and j-th tool face, and CPS_{ijk} is the k-th azimuth contribution in counts per second to CPS_{ij} given by

$$CPS_{ij} = \sum_{k=0^o}^{k=360^o} CPS_{ijk} \ , \tag{4.6}$$

with $CPS_{ijk} = CPS_{ij} \cdot FSF_k$ and FSF_k is the normalized one-dimensional azimuthal sensitivity function (middle panel of **Figures 3.2** and **3.3**) such that

$$\sum_{k=0^o}^{k=360^o} FSF_k = 1 \, . \tag{4.7}$$

Therefore, deconvolved sector measurements CPS_{ik} in counts per second are given by

$$CPS_{ik} = \sum_{j=0^o}^{j=360^o} CPS_{ijk} \ . \tag{4.8}$$

Equations 4.6-4.8 are the basis for azimuthal deconvolution of neutron detector count rates. For the synthetic model summarized in **Table 4.1**, LLNT count rates in an 8.5” borehole with 80^o well deviation are simulated with MCNP. Assuming a sampling rate of 0.5 ft and a 16-sector binning scheme, the results shown in **Figure 4.5** required 1560 hrs of computer time on a Linux workstation with dual Xeon 3 GHz processors for their calculation. We observe that deconvolved count rates in panels (b) and (d) correlate better to the formation bed boundary than the raw MCNP count rates shown in panels (a) and (c). Further, the ratio-method porosity obtained with deconvolution, shown in panel (f), is in better agreement with the bed boundary.

In the case of HA/HZ wells, azimuthal deconvolution corrects for the relatively large value of $\Delta\psi$ observed in neutron measurements while Δh depth shifts correct for image ΔD. Azimuthal deconvolution results shown in **Figure 4.5** are encouraging in that bed boundaries obtained from neutron count rates and porosity images are more accurate. This reduces errors in petrophysical interpretation when combined with density and gamma-ray measurements. In general, fast neutrons responses exhibit a larger EVOI than density responses but slow/thermal neutrons responses exhibit an EVOI which is on a par with the density response EVOI.

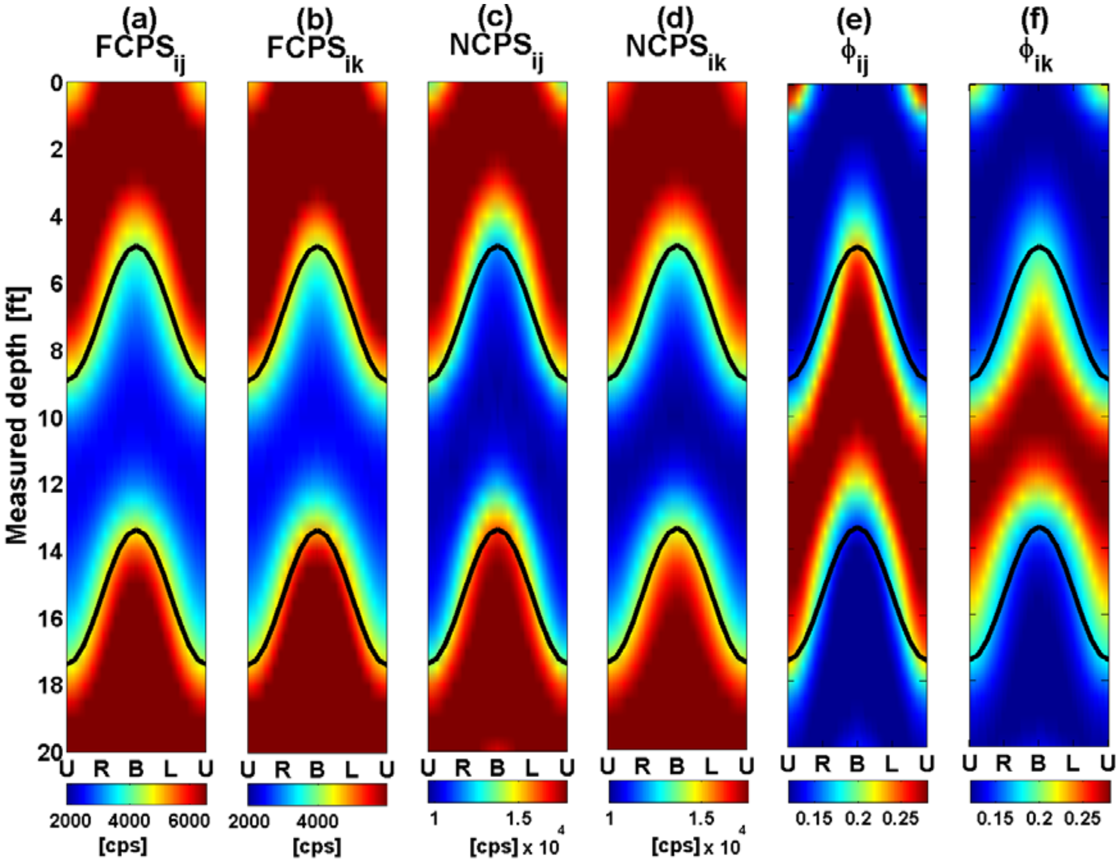

Figure 4.5: LLNT MCNP count rates in an 8.5” borehole with 80^o well deviation across formation properties described in Table 4.1. **(a)** Raw MCNP far-detector neutron count rates. **(b)** Deconvolved MCNP far-detector neutron count rates. **(c)** Raw MCNP near-detector neutron count rates. **(d)** Deconvolved MCNP near-detector neutron count rates. **(e)** Ratio-method porosity image from raw MCNP detector counts. **(f)** Ratio-method porosity image from deconvolved MCNP detector counts. Black solid curves represent true formation bed boundary.

4.3 THERMAL NEUTRON SENSITIVITY

Thermal neutron transport (below 0.41eV) in the vicinity of detectors is governed primarily by diffusion. The spatial FSF profiles of thermal neutrons shown in **Figure 3.3** indicate narrower *AR* than fast neutrons, hence higher vertical resolution. To illustrate this idea, we simulate LLNT MCNP measurements in 8.5" vertical and deviated wells across thin beds with the alternating formation layers described in **Table 4.1**. We compare porosity calculated from total neutrons i.e. thermal and epithermal, to porosity calculated from only thermal neutrons.

4.3.1 Vertical Wells

Figures 4.6 and **4.7** show LLNT MCNP logs numerically simulated in vertical wells across formations of varying layer thicknesses. In 3.5 ft beds (**Figure 4.6a-c**), thermal neutrons do not improve the resolution of the measurement because bed thickness is above the resolution of the measurements. In 1 ft (**Figure 4.6d-f**) and 0.5 ft beds (**Figure 4.7a-c**), thermal neutron porosity calibrated from far detector exhibits improved resolution. When bed thickness decreases to 0.25 ft (**Figure 4.7d-f**), both thermal and fast neutrons lose resolution because beds are much thinner than the resolution of the measurements.

4.3.2 High-angle Wells, 80^o dip

The cases shown in **Figures 4.6d-f** and **4.7a-c** are repeated for an 80^o well i.e. 1 ft and 0.5 ft. Porosity images and logs for fast and thermal neutrons are compared in **Figures 4.8** and **4.9**. We observe that porosity resolution is improved by thermal neutrons in deviated wells across thin beds, thereby reducing shoulder-bed effects. It is worth noting that the difference in *AR* between thermal and fast neutron responses is higher in the far detector than in the near detector.

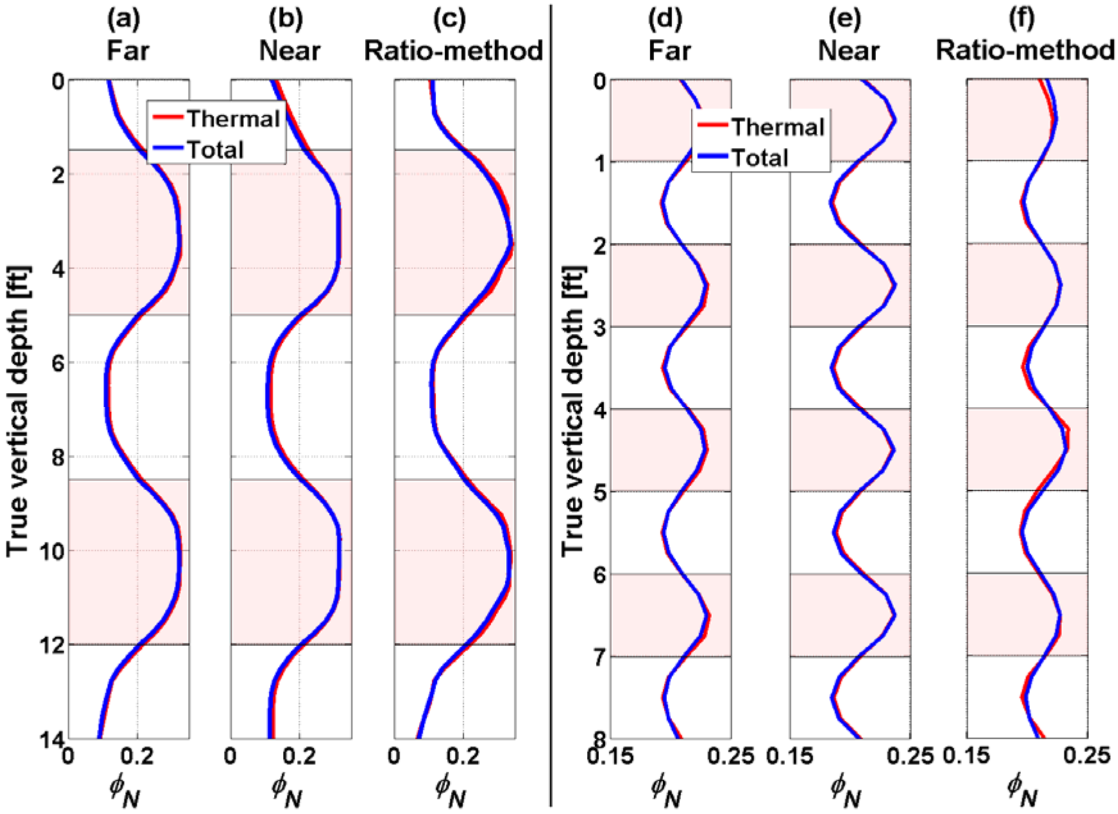

Figure 4.6: LLNT MCNP-simulated logs in an 8.5” vertical well across the formation model described in Table 4.1 with layer thicknesses of 3.5 ft (tracks 1-3) and 1.0 ft (tracks 4-6) and sampling rate of 0.25 ft. **(a)** Far-detector calibrated porosity showing thermal neutron porosity in red and total neutron porosity in blue. High-porosity layer I is shaded in orange while low-porosity layer II is shaded in white. **(b)** Same as (a) but for near detector. **(c)** Same as (a) but for ratio-method neutron porosity.

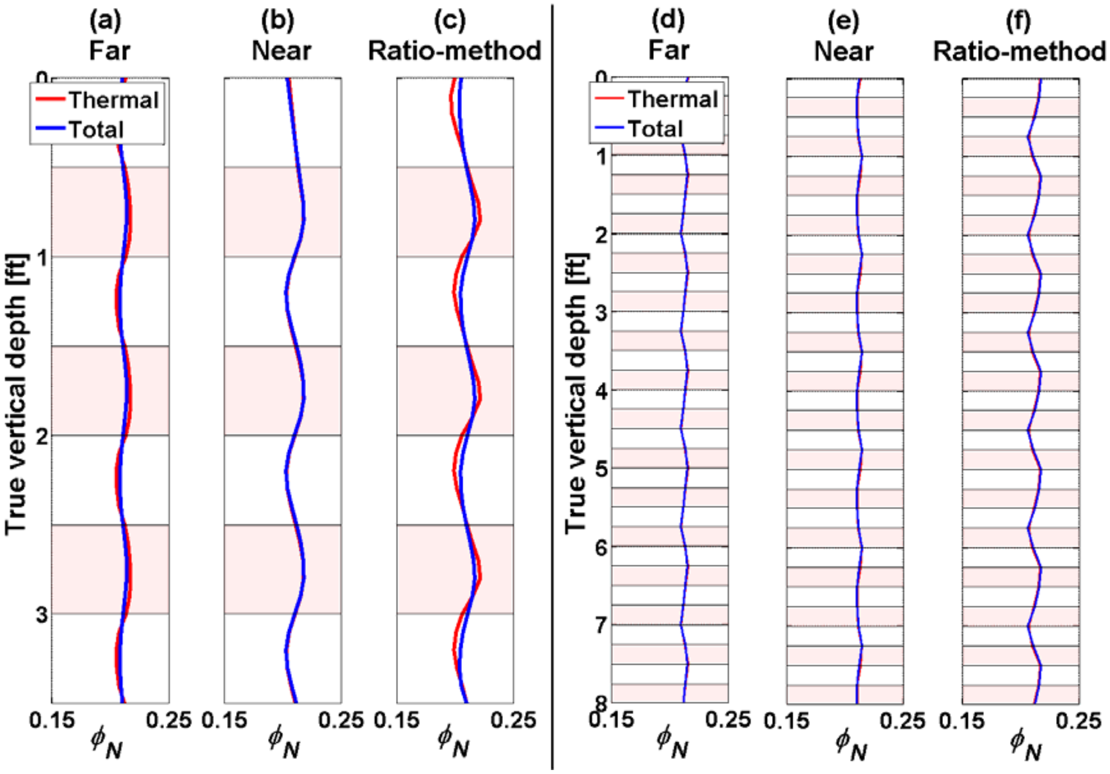

Figure 4.7: LLNT MCNP-simulated logs in an 8.5" vertical well across the formation model described in Table 4.1 with layer thicknesses of 0.5 ft (tracks 1-3) and 0.25 ft (tracks 4-6) and sampling rate of 0.1 ft. **(a)** Far-detector calibrated porosity showing thermal neutron porosity in red and total neutron porosity in blue. High-porosity layer I is shaded in orange while low-porosity layer II is shaded in white. **(b)** Same as (a) but for near detector. **(c)** Same as (a) but for ratio-method neutron porosity.

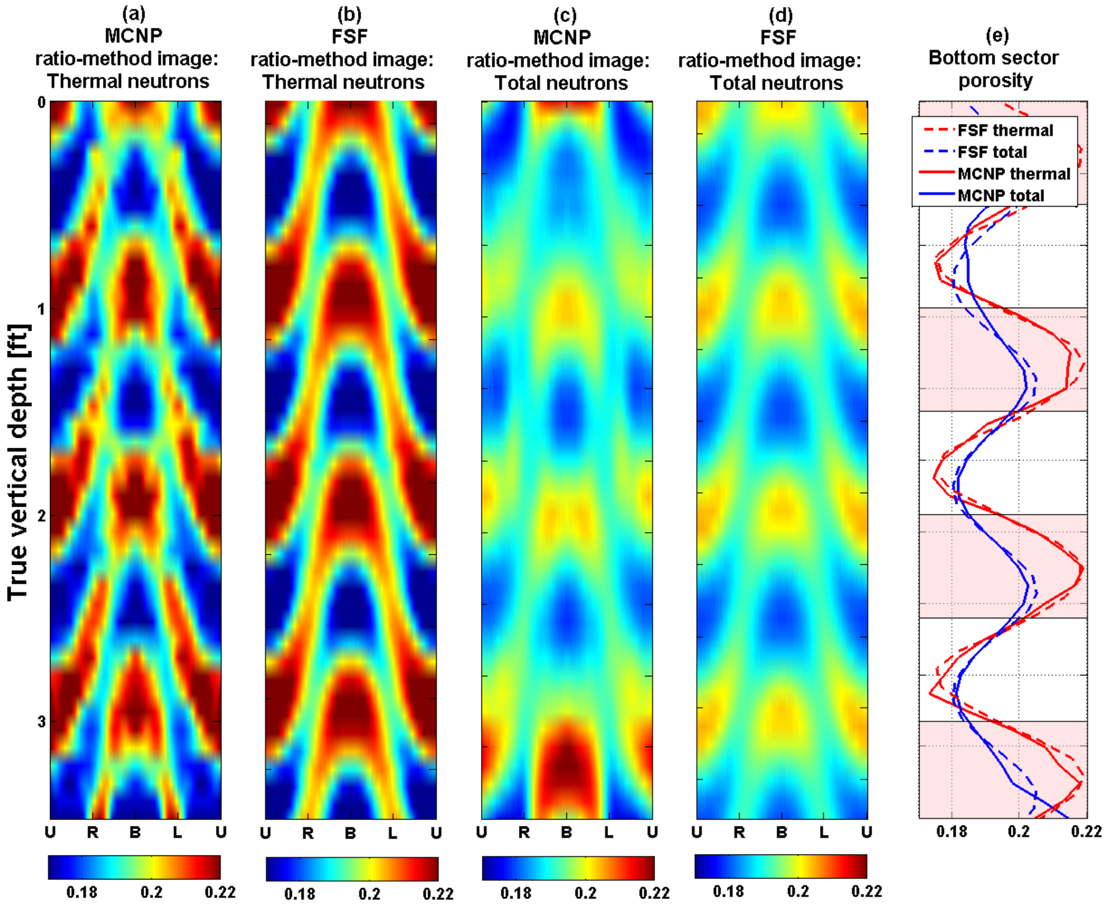

Figure 4.8: Comparison of MCNP and FSF LLNT simulations in an 8.5” well with 80^{o} well deviation across the formation model described in Table 4.1. Layer thicknesses are 0.5 ft; sampling rate is 0.5 ft in measured depth. **(a)** MCNP ratio-method porosity image for thermal neutrons. **(b)** FSF porosity image for thermal neutrons. **(c)** MCNP porosity image for total neutrons (fast and thermal). **(d)** FSF porosity image for total neutrons (fast and thermal). **(e)** Bottom quadrant porosity logs. High-porosity layer I is shaded in orange while low-porosity layer II is shaded in white.

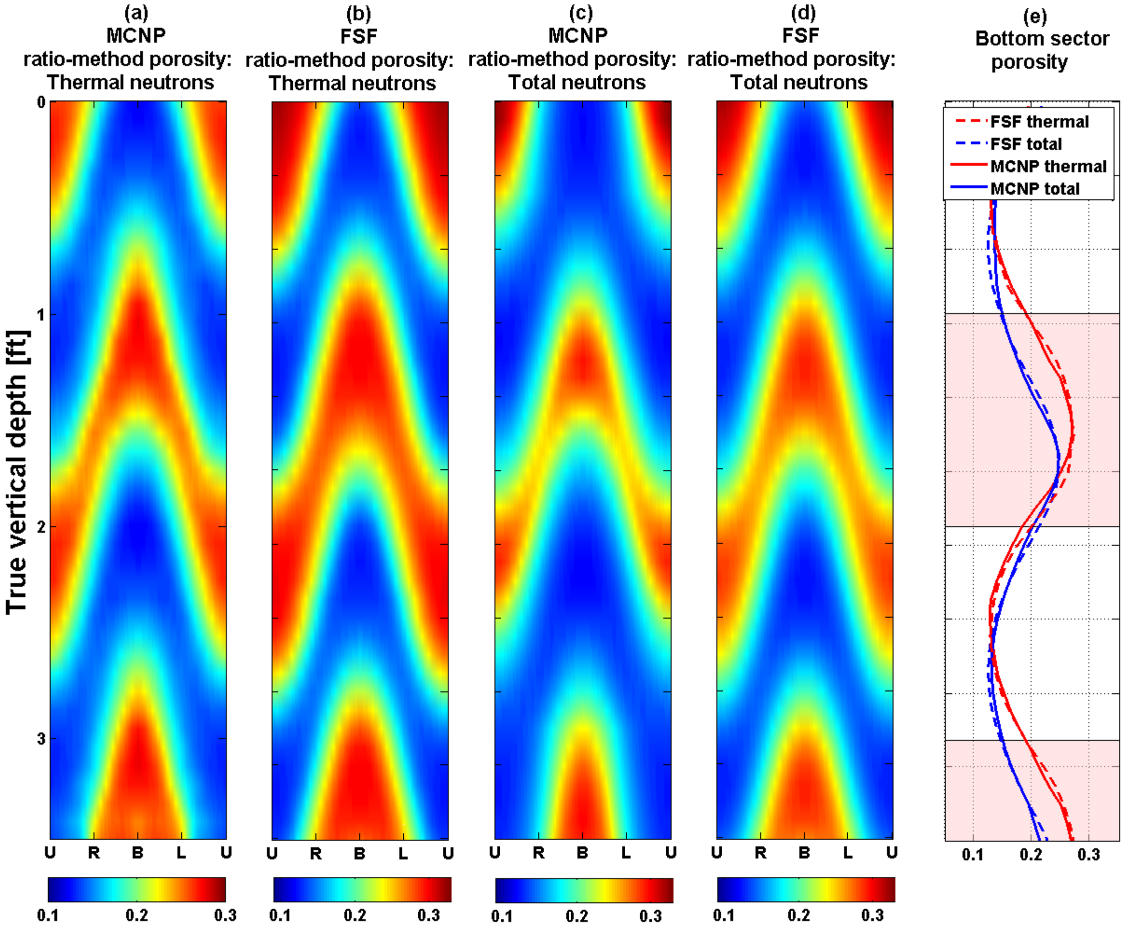

Figure 4.9: Comparison of MCNP and FSF LLNT simulations in an 8.5” well with 80^o well deviation across the formation model described in Table 4.1. Layer thicknesses are 1.0 ft; sampling rate is 0.5 ft in measured depth. **(a)** MCNP ratio-method porosity image for thermal neutrons. **(b)** FSF porosity image for thermal neutrons. **(c)** MCNP porosity image for total neutrons (fast and thermal). **(d)** FSF porosity image for total neutrons (fast and thermal). **(e)** Bottom quadrant porosity logs. High-porosity layer I is shaded in orange.

4.4 COMPARISONS OF NUMERICAL SIMULATIONS OF NEUTRON MEASUREMENTS PERFORMED WITH FSFS AND MCNP

Linear iterative refinement of pre-calculated FSFs is fast and accurate for interactive petrophysical modeling of wireline logs (Heidari et al., 2009; Mendoza et al., 2007; 2010a and b). Below we extend this method for its application to Longhorn LWD measurements.

As previously shown, neutron sensitivity parameters vary significantly with formation HI while gamma-ray sensitivity parameters are relatively constant. For this reason, linear iterative refinement of FSFs performs significant corrections in the case of neutron measurements. We also introduce the method of separate linear iterative refinement of energy-group FSFs. The inverse of the characteristic lengths governing particle transport at separate energy ranges is used as a weighting parameter. By splitting neutrons into thermal (below 0.41 keV) and fast/epithermal (above 0.41 keV) groups, we refine FSFs with inverses of L_d and L_s as weighting parameters, respectively. As shown in **Figures 3.2** and **3.3**, we observe a drastic reduction in AR from fast neutrons to thermal neutrons (8.2” in far detector and 4.4” in near detector). The value of AR is directly proportional to shoulder-bed effects. Hence we implement separate linear iterative refinement of thermal neutron FSFs with L_d as the weighting parameter to reduce shoulder-bed effects across thinly-bedded formations. **Figures 4.8** and **4.9** compare MCNP and FSF simulated neutron images for both thermal and fast neutrons. The MCNP simulations described in **Figures 4.8** and **4.9** required 1560 hrs of CPU time for their calculation on a Linux workstation with dual Xeon 3 GHz processors while the FSF results required 5 minutes on a Windows XP PC with dual-core 3.2 GHz processors. In comparison to MCNP, total/fast neutron FSF simulations yielded mean relative errors of 3.3% across 1 ft layers and 1.6% across 0.5 ft layers. Thermal neutron FSF simulations yielded mean relative errors of 3% across 1 ft layers and 1% across 0.5 ft layers. These errors are acceptable in view of the substantial improvement in simulation speed. Two-dimensional FSF maps of the Longhorn LWD tools are shown in Appendix A.

Chapter 5: Field Example of Geometrical and Petrophysical Interpretation

In this chapter, I apply the LWD measurement and interpretation techniques discussed in previous chapters to a field case. The goal is to show how integrated forward modeling improves the quantitative interpretation of LWD nuclear measurements across variable bed thicknesses and formation properties in HA/HZ wells. In thinly-bedded formations, false crossovers are a consequence of different EVOIs between density and neutron measurements. As shown with the cases described below, the techniques introduced in this thesis reduce this anomalous behavior.

5.1 INTEGRATED FORWARD MODELING OF FIELD CASE

The field case under consideration comprises the LWD measurements acquired in a HA/HZ well in West Africa and shown in **Figure 5.1**. The section shown in that figure is located below the free oil-water contact and mainly consists of calcite-cemented siltstones or silty limestones. Layers are thinly bedded with stratigraphic thicknesses between 0.5 and 2 ft. The well was drilled with an 8.5" collar and water-base mud and its trajectory varies from 78^o to 82^o. Track 5 of **Figure 5.1** describes the short-spaced image, which exhibits lower quality in the upper/top azimuths. This behavior implies that the tool is eccentered in the borehole.

Petrophysical analysis of available well logs (density, gamma ray, neutron, PEF and resistivity) was carried out to determine matrix and fluid volumes. Additionally, geometrical interpretations were performed to calculate layer thicknesses and formation dips from compensated density images. Results from these analyses define the earth-model which consists of multi-layer values of porosity, water saturation, and matrix volumes (sand, shale, and calcite). Layer-by-layer values of bulk density, characteristic lengths, and PEF were calculated with the Schlumberger Nuclear Parameter code (SNUPAR, McKeon et al., 1989). LWD density, PEF, neutron and gamma ray measurements were then simulated with the FSF rapid simulation technique, followed by the image processing and correction techniques discussed earlier. Simulated measurements were contaminated with 5% Gaussian noise in an effort to mimic uncertainties due noisy field measurements. Petrophysical and geometrical analyses were performed on the simulated well logs and the resulting earth-model compared to the initial earth-model. This process was carried out iteratively until securing the best possible match between measurements and numerical simulations. **Figure 5.2** describes the integrated forward modeling approach for interpretation of LWD nuclear measurements.

Figure 5.3 shows the final, numerically simulated LWD nuclear measurements (images and logs), assuming the Longhorn tool models. Tracks 5-8 in that figure compare bottom quadrant simulated logs to field measurements. Discrepancies can be attributed to differences in measurement resolution and response characteristics, particularly across thinly-bedded formations, between the Longhorn tools and the commercial tools used in this well. These discrepancies are quantified in mean absolute errors. We observe mean errors of 0.036 g/cc, 0.15 b/e, 0.034, and 7.5 gapi between simulated and field density, PEF, neutron porosity, and gamma ray measurements respectively.

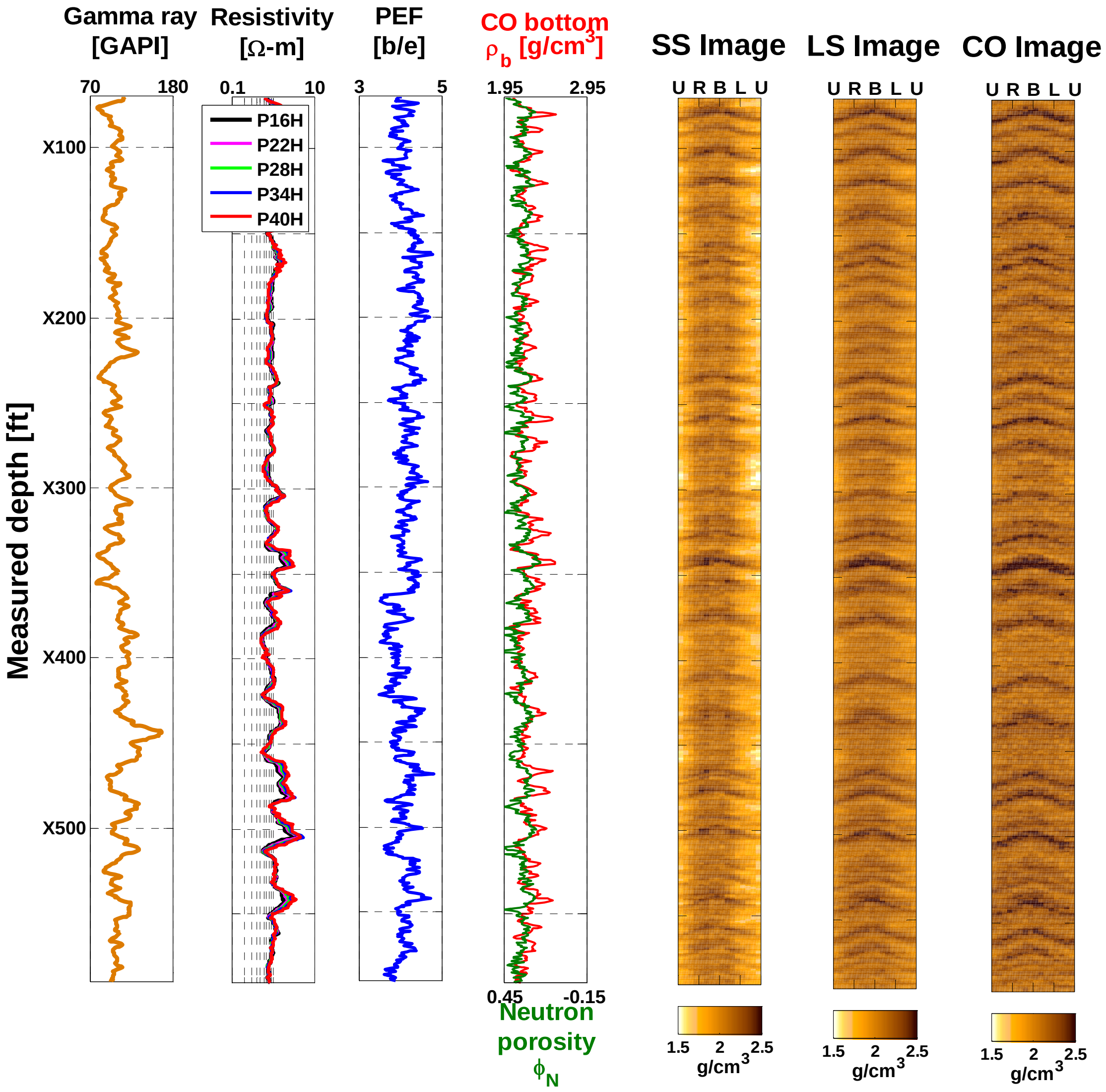

Figure 5.1: Field LWD measurements acquired in a high-angle well across thinly-bedded formations. **(a)** Track 1 shows gamma ray log. (**b**) Track 2 shows resistivity measurements. (**c**) Track 3 shows PEF measurement. (**d**) Track 4 shows bottom sector compensated density measurement in red and neutron porosity in green. (**e**) Track 5 shows short-spaced density image. (**f**) Track 6 shows long-spaced density image. (**g**) Track 7 shows compensated density image. Upper (U), right (R), left (L), and bottom (B) azimuths are shown for reference.

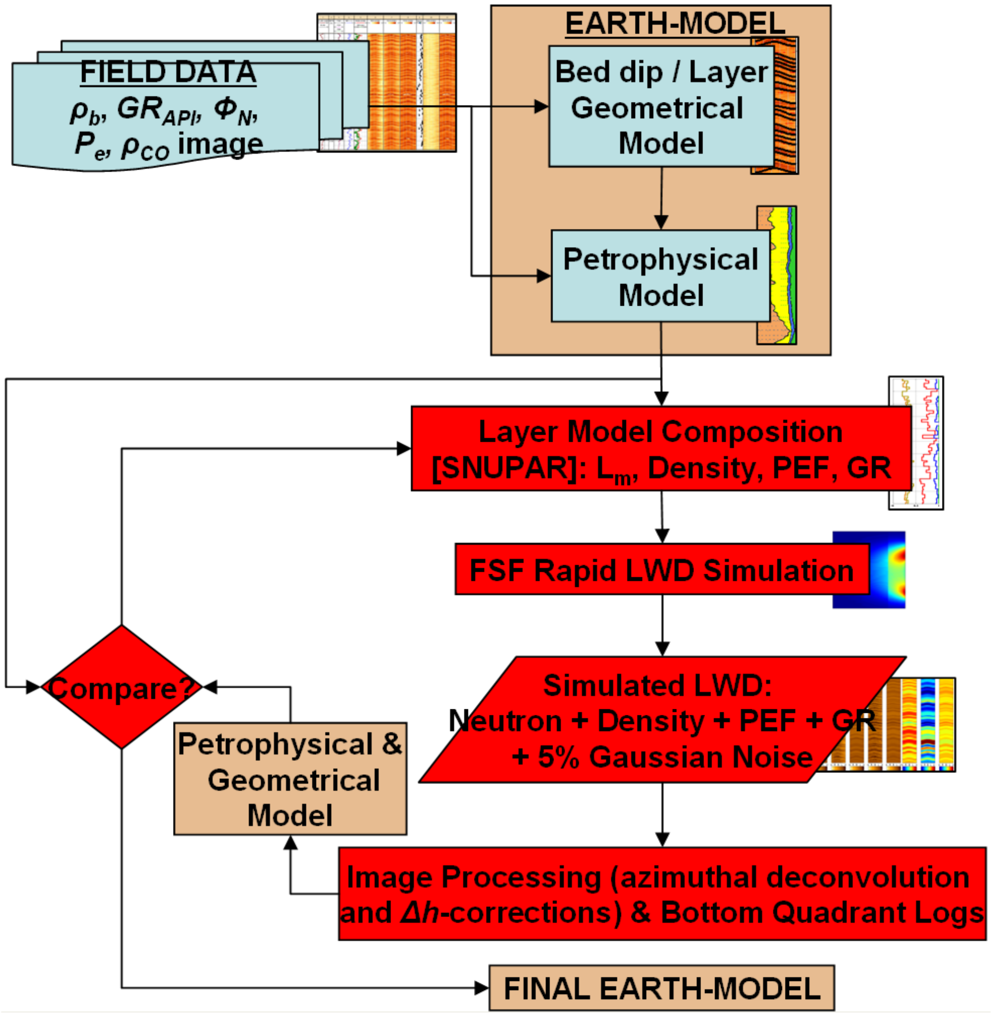

Figure 5.2: Flowchart of the integrated petrophysical and geometrical forward modeling method.

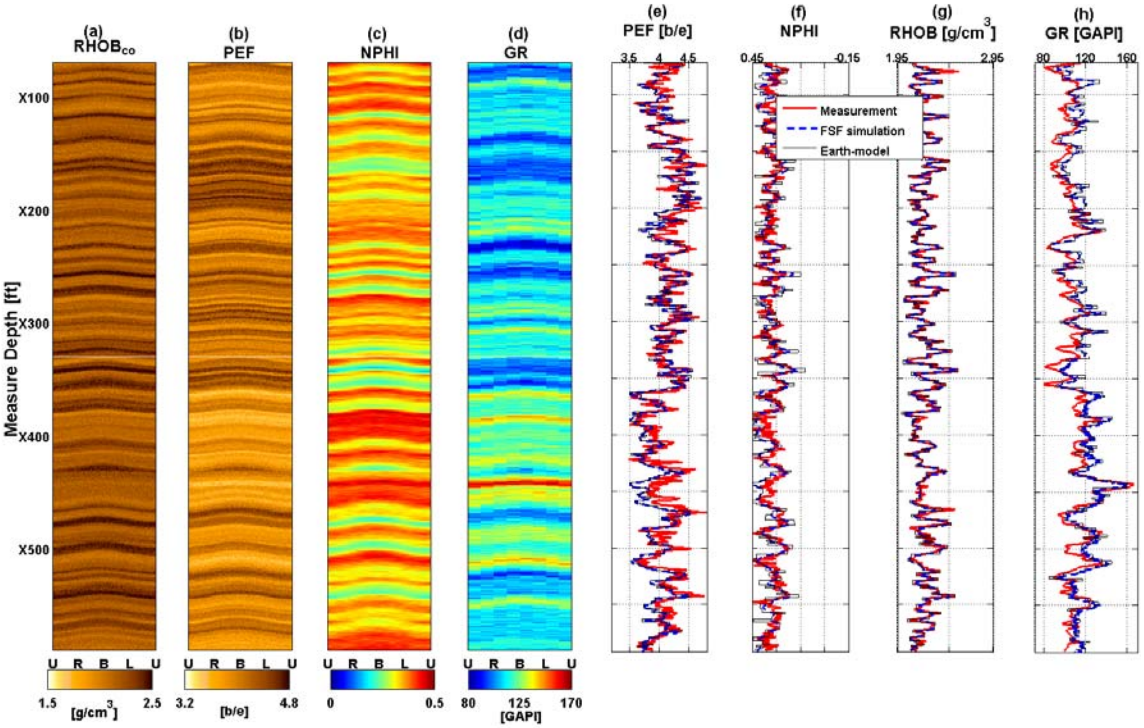

Figure 5.3: Final FSF-simulated LWD nuclear measurements for the field case using the Longhorn tools. **(a)** Simulated compensated density image, $RHOB_{co}$. **(b)** Simulated *PEF* image. **(c)** Simulated ratio-method neutron porosity image, NPHI. **(d)** Simulated gamma ray image, *GRAPI*. **(e)** Simulated bottom quadrant *PEF* log (dashed blue), field *PEF* measurement (solid red), and earth-model calculated *PEF* (blocked black). **(f)** Same as (e) but for neutron porosity. **(g)** Same as (e) but for bulk density. **(h)** Same as (e) but for spontaneous gamma ray.

5.2 FORWARD MODELING OF A FIELD-BASED SYNTHETIC CASE

To further explore petrophysical and geometrical effects on LWD nuclear measurements, we modify the well trajectory and layer properties in the earth-model within practical petrophysical and geometrical limits.

5.2.1 Clean/shale-stripped Model

To investigate false neutron-density crossovers across thinly-bedded formations, we strip the model of its shale content i.e. the volumetric concentration of shale (C_{sh}) in the earth-model is uniformly set to zero. This implies that shale matrix is replaced with sand and total porosity in the modified earth-model reduces to

$$\phi_t' = \phi_t - C_{sh}\phi_{sh} , \tag{5.1}$$

where ϕ_t' is total porosity in the modified earth model, ϕ_t is total porosity in the original earth model, C_{sh} is the volumetric concentration of shale in the original earth-model, and ϕ_{sh} is shale porosity. The well trajectory is also changed to vary from vertical at the top of the earth model to horizontal at the bottom.

Figure 5.4 shows the corresponding forward modeling results for this case. Track 7 shows compensated density ($RHOB_{co}$) and ratio-method neutron porosity (*NPHI*) logs plotted on a limestone water-filled porosity scale. Despite being water saturated, we observed neutron-density crossovers across the layers. As shown in track 8 of **Figure 5.4**, enhanced (alpha-processed) neutron (*NPOR*) and enhanced density (*NRHO*) logs minimize the crossovers. From track 9 of the same figure, we observe that the simulation method of separate iterative refinement on thermal group FSF to yield thermal-neutron enhanced porosity log (*NPOR'*) eliminates most of the neutron-density crossovers. To quantify the effect of enhancing neutron sensitivity, we re-interpreted total porosity from numerically simulated logs and compared to layer-by-layer porosity values. **Table 5.1** summarizes the average absolute errors. The method of separate iterative refinement on thermal neutrons reduces the average absolute error in porosity estimation by 5%.

Density + Neutron	**Absolute error [%]**
$RHOB_{co} + NPHI$	20.1
$NRHO + NPOR$	17.3
$NRHO + NPOR'$	15.2

Table 5.1: Average absolute errors between re-interpreted porosity from simulated logs and earth-model porosity. $RHOB_{co}$ is compensated density measurement, *NRHO* is enhanced (alpha-processed) density measurement, *NPHI* is ratio-method neutron porosity, *NPOR* is enhanced (alpha-processed) neutron porosity, and *NPOR'* is enhanced thermal neutron porosity from separate iterative refinement of thermal-group FSF.

5.2.2 Shaly Model

To investigate the effect of shale in the model, we set volumetric shale concentration values back to those of the initial earth model. **Figures 5.5** and **5.6** show the corresponding modeling results for this case. At approximately 160 ft in the horizontal section of the well, false neutron-density crossovers are completely eliminated in **Figure 5.6** due to enhanced porosity resolution using separate iterative refinement on thermal neutron FSFs.

It is worth mentioning that along the depth interval between 20-40 ft the PEF image shown in track 2 of **Figures 5.4-5.6**, exhibits the best resolution across thin beds. Layers within this depth interval are less than 1 ft in thickness and are below the resolution of LWD neutron measurements. Using thermal FSF refinement, we observe a reduction in shoulder-bed effects across this depth interval.

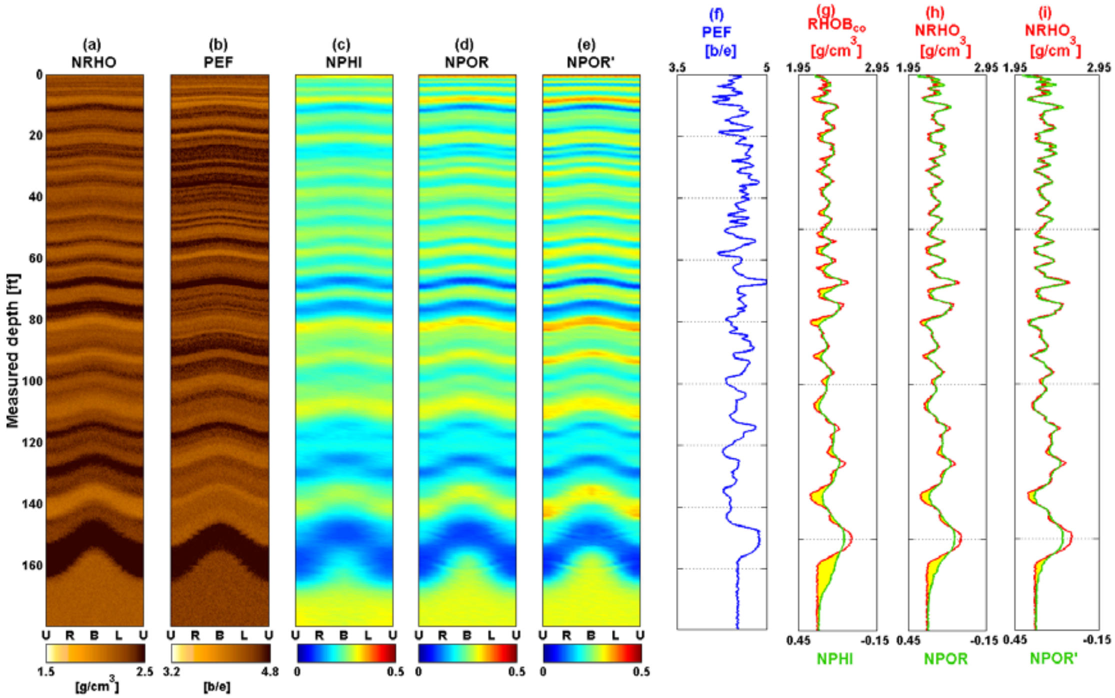

Figure 5.4: Field-based, shale-stripped model simulation results. **(a)** Simulated enhanced (alpha-processed) density image, *NRHO*. **(b)** Simulated *PEF* image. **(c)** Simulated ratio-method neutron porosity image, *NPHI*. **(d)** Simulated enhanced neutron porosity image, *NPOR*. **(e)** Simulated enhanced neutron porosity image using separate iterative refinement on thermal neutron sensitivity, *NPOR'* **(f)** Bottom quadrant *PEF* log. **(g)** Bottom quadrant compensated density log, $RHOB_{co}$ (red curve) and bottom quadrant ratio-method neutron porosity log, *NPHI* (green curve). **(h)** Bottom quadrant enhanced (alpha-processed) density log, *NRHO* (red curve) and bottom quadrant enhanced (alpha-processed) neutron porosity log, *NPOR* (green curve). **(i)** Bottom quadrant enhanced (alpha-processed) density log, *NRHO* (red curve) and bottom quadrant *NPOR'* (green curve).

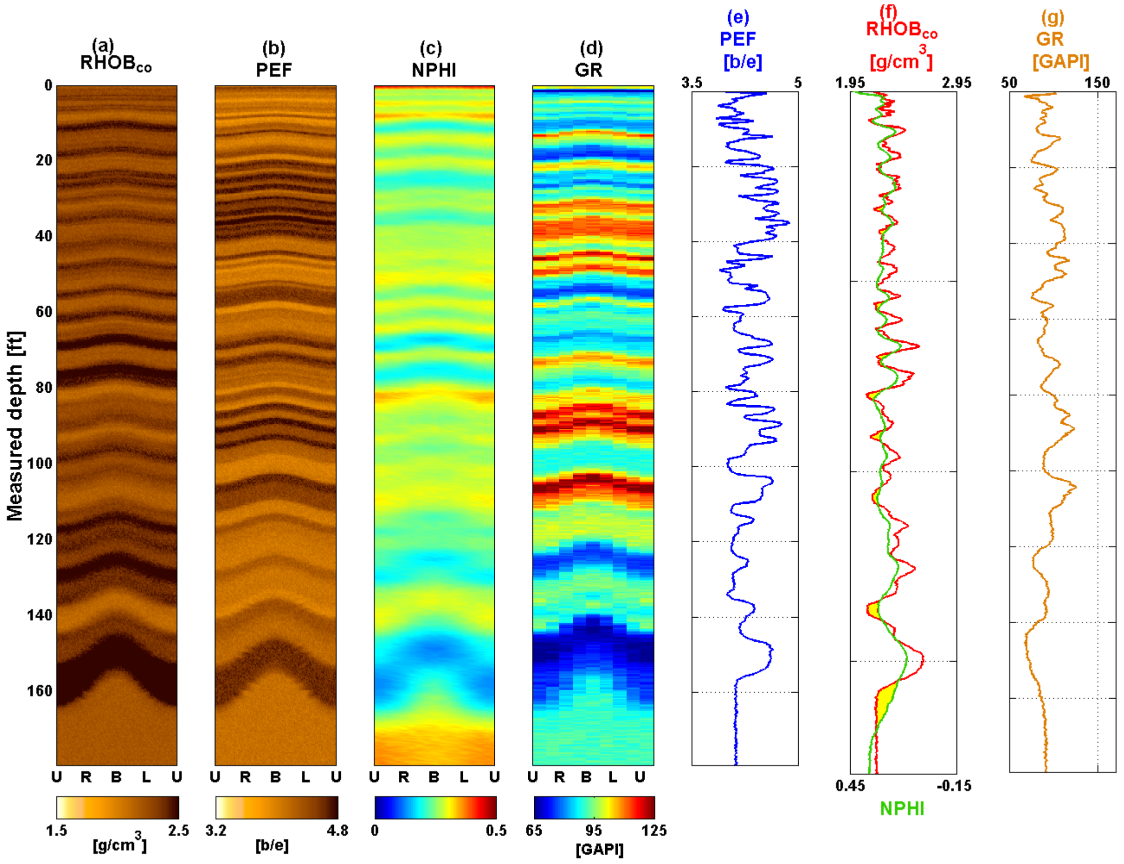

Figure 5.5: Field-based, shaly-model simulation results. **(a)** Simulated compensated density image, $RHOB_{co}$. **(b)** Simulated photoelectric factor image, *PEF*. **(c)** Simulated ratio-method neutron porosity image, *NPHI*. **(d)** Simulated spontaneous gamma ray image, *GRAPI*. **(e)** Bottom quadrant photoelectric factor log, *PEF*. **(f)** Bottom quadrant compensated density log, $RHOB_{co}$ (red curve) and bottom quadrant ratio-method neutron porosity log, *NPHI* (green curve). **(g)** Bottom quadrant spontaneous gamma ray log, *GR*.

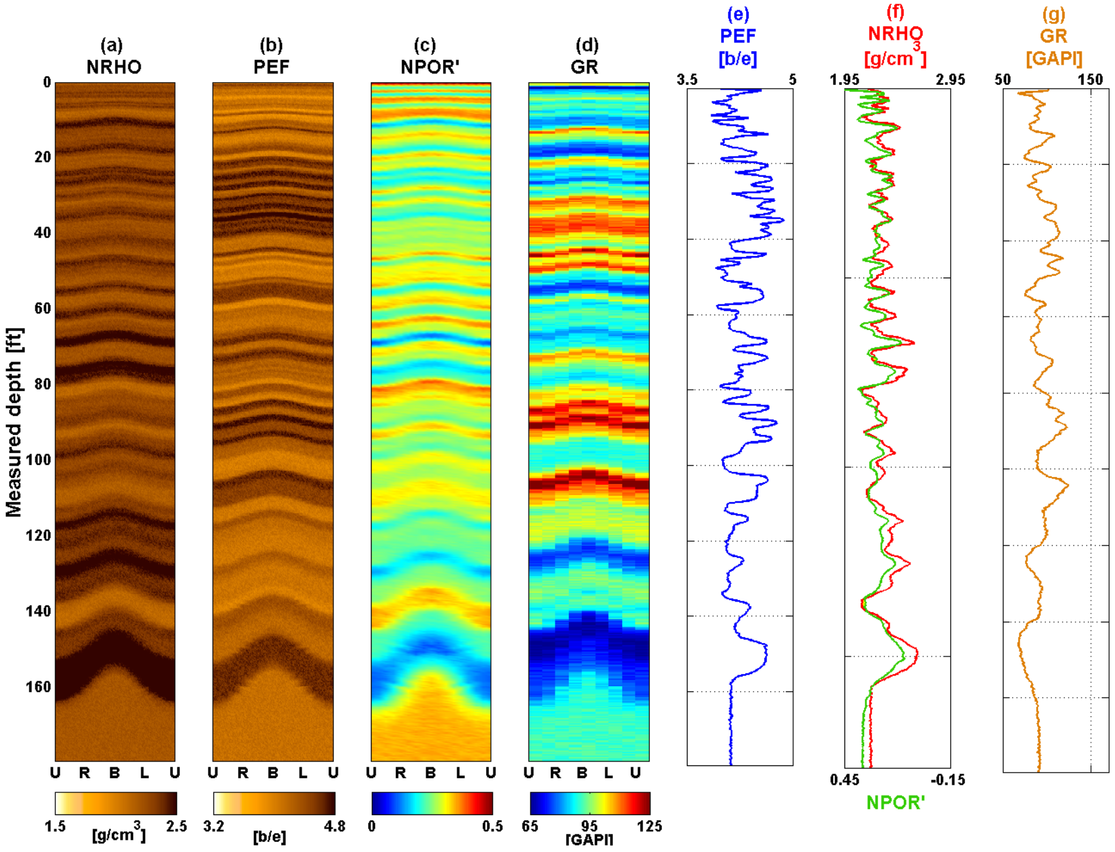

Figure 5.6: Field-based, shaly-model simulation results. **(a)** Simulated enhanced (alpha-processed) density image, *NRHO*. **(b)** Simulated photoelectric factor image, *PEF*. **(c)** Simulated enhanced (separate iterative refinement on thermal neutron FSF) neutron porosity image, *NPOR'*. **(d)** Simulated spontaneous gamma ray image, *GRAPI*. **(e)** Bottom quadrant photoelectric factor log, *PEF*. **(f)** Bottom quadrant enhanced (alpha-processed) density log, *NRHO* (red curve) and bottom quadrant enhanced (separate iterative refinement on thermal neutron FSF) neutron porosity image, *NPOR'* (green curve). **(g)** Bottom quadrant spontaneous gamma ray log, *GR*.

Chapter 6: Summary, Conclusions, and Recommendations

6.1 SUMMARY AND CONCLUSIONS

The effect of tool eccentricity cannot be ignored in LWD measurements. In an 80^o well, a 3^o dip estimation error was observed without tool eccentricity corrections. We observed a 5% porosity improvement with our forward modeling technique by enhancing neutron porosity resolution across thinly-bedded formations. Monte Carlo simulations of multi-sector LWD measurements in HA/HZ wells could take days to weeks. The FSF simulation method introduced in this thesis is accurate to below 3% relative error in thin beds and drastically reduces computation time from days to minutes.

In this thesis, we characterized flux responses of LWD nuclear measurements in term of geometrical sensitivity parameters (ΔD, ΔR, and $\Delta\psi$) for centered and eccentered tools. Our understanding of these parameters assisted in developing image correction techniques in the presence of tool eccentricity to improve formation dip estimation from density images. We observed that the neutron $\Delta\psi$ value is 6 times larger than the gamma $\Delta\psi$ value. This property prompted us to advance the method of azimuthal deconvolution in neutron image processing methods for improved bed boundary correlation and porosity estimation. These advances serve as ground work for development of neutron inversion techniques. Using the FSF rapid simulation method, we developed and successfully tested an integrated forward modeling approach for the interpretation of LWD nuclear measurements with simulated measurements matching field data to an acceptable degree. Mean errors of 0.036 g/cc, 0.15 b/e, 0.034, and 7.5 gapi between simulated and field density, PEF, neutron porosity, and gamma ray measurements, respectively, were obtained for the field case. These errors can be reduced further by modeling the measurements with the actual commercial tools used in the well. We also observed that simulated PEF images give the best vertical resolution, below 1 ft of bed thickness.

Nuclear measurements exhibit significantly different EVOIs. Quantitative understanding of these EVOIs is necessary to appropriately correct nuclear measurements before their combined petrophysical interpretation. This requires that measurement responses be on par in terms of the corresponding sensitivity volumes for reliable geometrical and petrophysical estimations. It was shown that AR decreases by 8.2” for the far detector and 4.4” for the near detector from fast to thermal neutrons. This causes a reduction of shoulder-bed effects and hence of false crossovers. It is also equivalent to a 5% reduction in porosity error, as shown with the field-based synthetic case. Consistent bed boundary prediction among nuclear measurements is also essential. Rapid integrated forward modeling enables the quantitative synthesis of the various measurement responses for estimation of petrophysical and geometrical formation properties. The field example indicated that reliability of petrophysical interpretation and confidence in predicted formation properties can be improved through numerical simulation. Our implementation of the FSF rapid simulation method is an important step toward inverse modeling of LWD nuclear measurements in thinly-bedded formations.

6.2 RECOMMENDATIONS

The following list of recommendations will expand the research work described in this thesis:

i) The study of LWD responses in boreholes of non-circular shapes e.g. elliptic boreholes, to characterize the effects on petrophysical interpretation.

ii) Operability of the fast modeling approach encourages development of inversion methods. Integrated inversion techniques could be developed for multi-sector LWD nuclear measurements (density, PEF, neutron and gamma ray) to obtain petrophysical and geometrical formation properties. This would further improve our understanding of LWD response characteristics.

iii) The incorporation of resistivity measurements for forward and inverse modeling would enable accurate porosity and saturation prediction.

Appendix A: Longhorn LWD Tools' Calibration Plots and Flux Maps

Modeling of commercial LWD tools is unavailable because of proprietary protection on design technology. The Longhorn generic models were developed to resemble published tool response data. In this appendix, I show calibration plots and two-dimensional sensitivity maps of the Longhorn LWD tools.

A.1 CALIBRATION PLOTS

Figure A.1 shows the LLDT spine-and-rib plots used for standoff compensation.

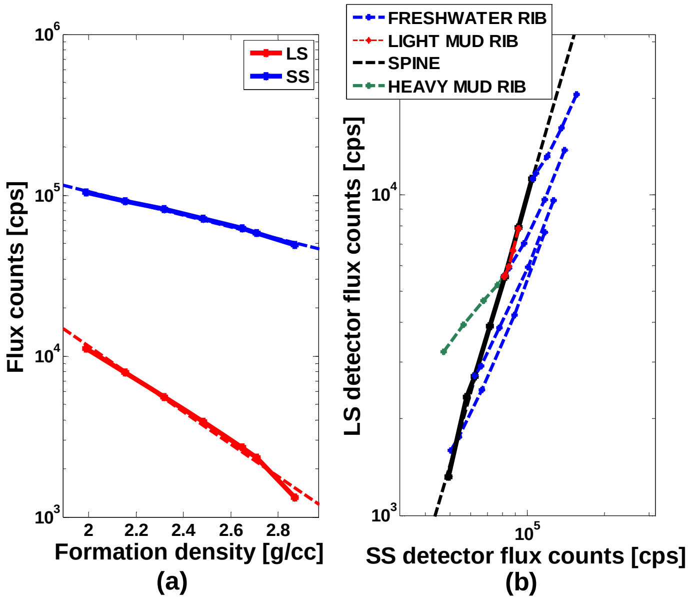

Figure A.1: **(a)** Long-spaced (red) and short-spaced (blue) detector flux counts of LLDT. **(b)** Spine-and-ribs plots of LLDT freshwater, light-mud, and heavy-mud. Light-mud consists of oil-base mud with 50% barite while heavy-mud consists of water-base mud with 50% barite.

In **Figure A.2**, we show the LLNT near and far detectors counts versus limestone porosity. The counts ratio-to-porosity transform of the LLNT is compared to that of the neutron porosity sub, NPS (Evans et al., 1988).

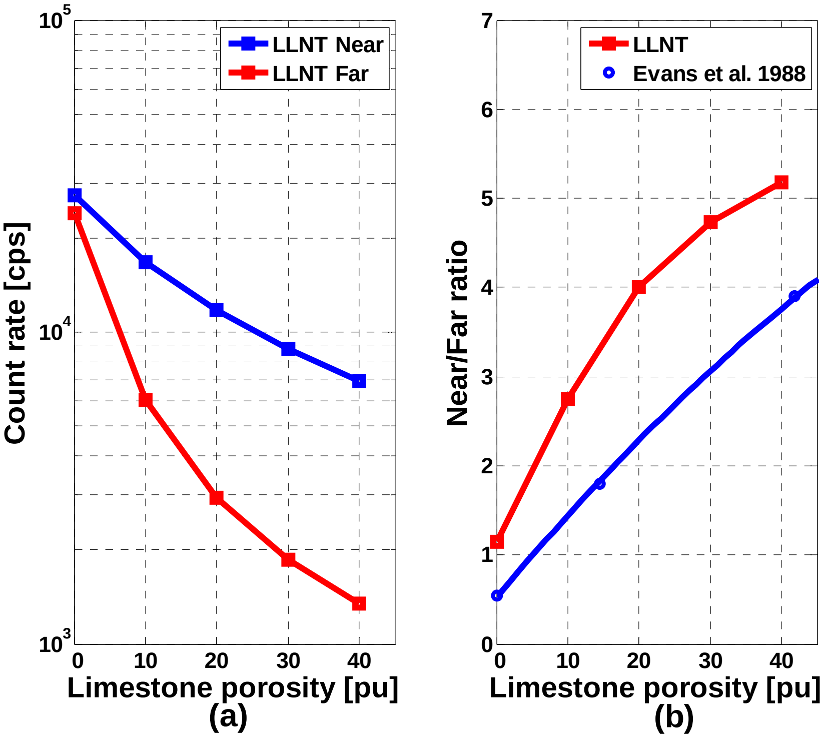

Figure A.2: **(a)** LLNT detector count rates versus water-filled limestone porosity (p.u.) **(b)** Near-to-far counts ratio versus porosity in water-filled limestone for LLNT and neutron porosity sub, NPS (Evans et al., 1988). It is worth noting that the NPS tool uses an Americium-Beryllium chemical source and was modeled in a 6.5-inch drill collar while LLNT uses a 14 MeV source in an 8.5-inch drill collar.

Figure A.3 shows the LLGT simulated pulse spectra for uranium, thorium, and potassium in an 8.5-inch water-filled borehole across a 2.41 g/cc kaolinite formation.

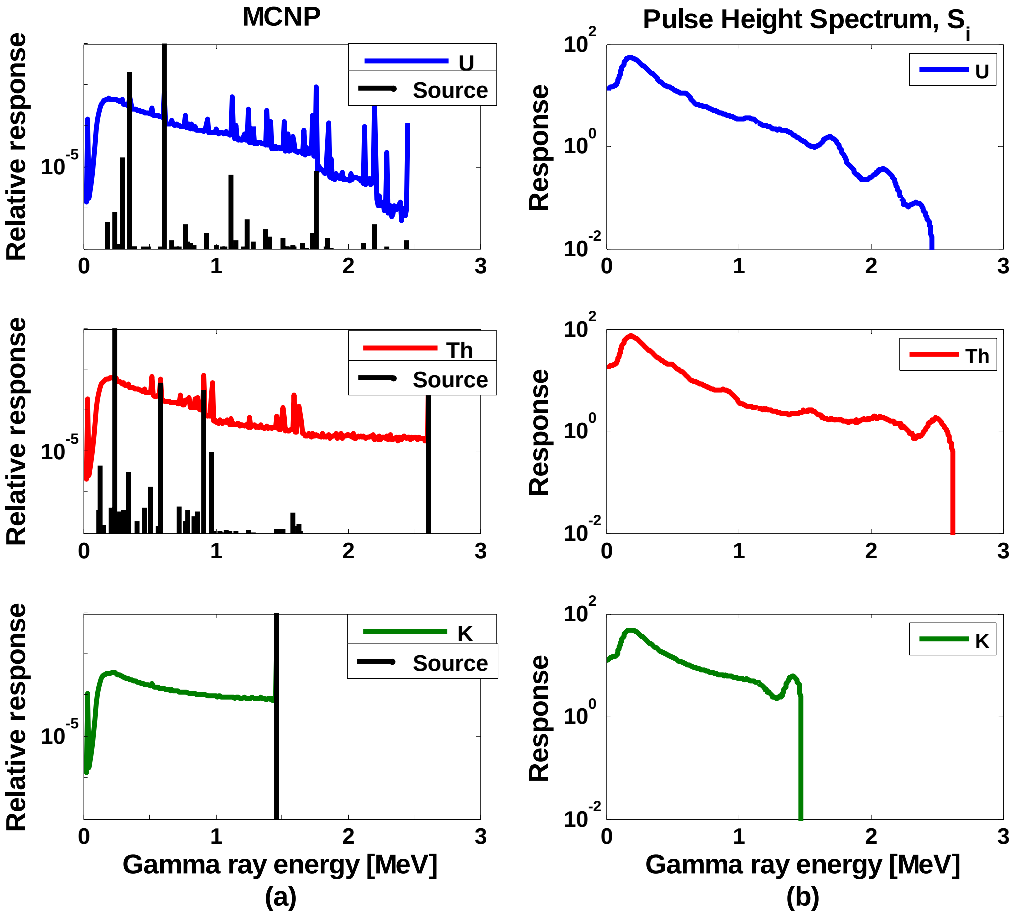

Figure A.3: **(a)** MCNP simulation response of LLGT in an 8.5-inch water-filled borehole across a 2.41 g/cc kaolinite formation. The black spectra lines represent the distribution of gamma rays from the formation's naturally occurring radiation. **(b)** Pulse height spectra, S_i of LLGT in an 8.5-inch water-filled borehole across a 2.41 g/cc kaolinite formation obtained by the convolution of MCNP simulated responses and pulse height map. The results obtained here are in good agreement with published tool responses (Mendoza et al., 2006).

Tables A1-A3 summarize formation base cases for density, neutron, and gamma ray tools.

LLDT base cases	Formation density [g/cc]	Formation composition
I	2.870	$CaMg(CO_3)_2$
II	2.710	$CaCO_3$
III	2.650	SiO_2
IV	2.480	0.9 SiO_2 + 0.1 H_2O
V	2.320	0.8 SiO_2 + 0.2 H_2O
VI	2.155	0.7 SiO_2 + 0.3 H_2O
VII	1.990	0.4 SiO_2 + 0.4 H_2O

Table A.1: Base case formation densities and compositions for Longhorn LWD density tool (LLDT).

LLNT base cases	Formation porosity [pu]	Formation composition	Characteristic lengths [cm]		
			L_d	L_s	L_m
I-I	40	0.6 SiO_2 + 0.4 CH_4	26.68	37.53	46.84
I-II	30	0.7 SiO_2 + 0.3 CH_4	24.26	34.72	43.10
I-III	20	0.8 SiO_2 + 0.2 CH_4	22.25	32.64	40.20
I-IV	0	SiO_2	19.09	29.98	36.20
I-V	10	0.9 SiO_2 + 0.1 H_2O	11.82	17.54	21.46
I-VI	20	0.8 SiO_2 + 0.2 H_2O	8.62	15.07	17.56
I-VII	30	0.7 SiO_2 + 0.3 H_2O	6.80	13.88	15.60
I-VIII	40	0.6 SiO_2 + 0.4 H_2O	5.62	13.21	14.46

II-I	40	0.6 $CaCO_3$ + 0.4 CH_4	19.67	33.83	39.78
II-II	30	0.7 $CaCO_3$ + 0.3 CH_4	17.63	30.91	36.18
II-III	20	0.8 $CaCO_3$ + 0.2 CH_4	15.98	28.66	33.37
II-IV	0	$CaCO_3$	13.46	25.46	29.31
II-V	10	0.9 $CaCO_3$ + 0.1 H_2O	9.49	16.36	19.18
II-VI	20	0.8 $CaCO_3$ + 0.2 H_2O	7.4	14.26	16.24
II-VII	30	0.7 $CaCO_3$ + 0.3 H_2O	6.09	13.27	14.73
II-VIII	40	0.6 $CaCO_3$ + 0.4 H_2O	5.19	12.74	13.85
III-I	40	0.6 $CaMg(CO_3)_2$+ 0.4 CH_4	22.30	30.15	38.04
III-II	30	0.7 $CaMg(CO_3)_2$+ 0.3 CH_4	20.05	27.30	34.37
III-III	20	0.8 $CaMg(CO_3)_2$+ 0.2 CH_4	18.21	25.10	31.47
III-IV	0	$CaMg(CO_3)_2$	15.38	21.90	27.18
III-V	10	0.9 $CaMg(CO_3)_2$+ 0.1 H_2O	10.52	15.09	18.63
III-VI	20	0.8 $CaMg(CO_3)_2$+ 0.2 H_2O	83.01	13.40	15.78
III-VII	30	0.7 $CaMg(CO_3)_2$+ 0.3 H_2O	6.47	12.61	14.29
III-VIII	40	0.6 $CaMg(CO_3)_2$+ 0.4 H_2O	5.43	12.20	13.44

Table A.2: Base case formation porosities, compositions and characteristic lengths for Longhorn LWD neutron tool (LLNT).

LLGT base cases	Formation density [g/cc]	Formation composition	Isotope
I	2.41	Kaolinite, $Al_4Si_4O_{10}(OH)_8$	Uranium-238
II	2.41	Kaolinite, $Al_4Si_4O_{10}(OH)_8$	Thorium-232
III	2.41	Kaolinite, $Al_4Si_4O_{10}(OH)_8$	Potassium-40

Table A.3: Base case formation density, composition and isotope radiation for LLGT.

A.2 TWO-DIMENSIONAL FLUX SENSITIVITY MAPS

Figures A4-A6 show the two-dimensional FSF maps for the Longhorn LWD tools.

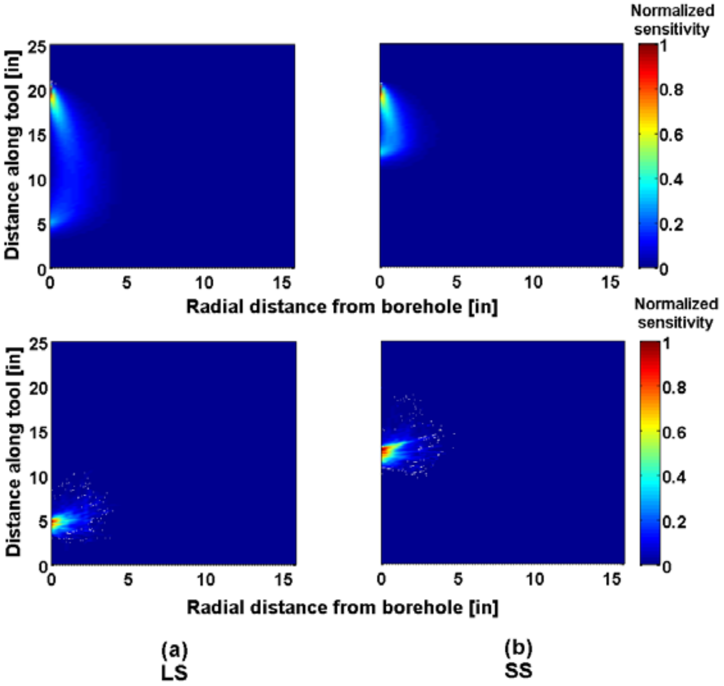

(a)
LS

(b)
SS

Figure A.4: LLDT 2-D normalized FSF map in a 2.32 g/cc formation. **(a)** Top panel shows long-spaced detector sensitivity map for Compton scattering while bottom map shows sensitivity map for photoelectric effect. **(b)** Same as (a) but for short-spaced detector.

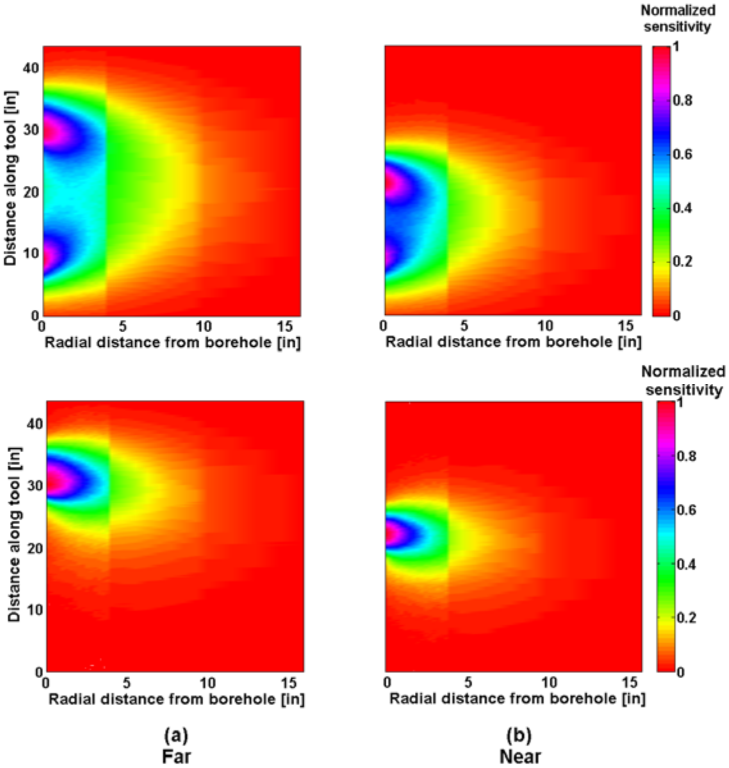

Figure A.5: LLNT 2-D normalized FSF map in a 20 p.u. water-filled formation. **(a)** Top panel shows far detector sensitivity map for fast neutrons while bottom map shows sensitivity map for thermal neutrons. **(b)** Same as (a) but for near detector.

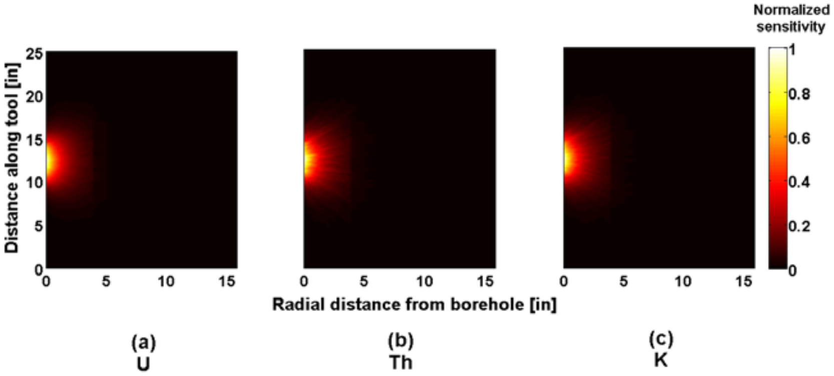

Figure A.6: LLGT 2-D normalized FSF map in a 2.41g/cc kaolinite formation. **(a)** Spontaneous gamma ray sensitivity response to Uranium radiation isotope. **(b)** Same as (a) but for Thorium isotope. **(c)** Same as (a) but for Potassium isotope.

List of Symbols

A	Location of image crest
A'	Location of corrected image crest
A_{api}	Uranium API calibration coefficient
A_r	Atomic weight
AR	Axial resolution [in]
B	Location of image trough
B'	Location of corrected image trough
B_{api}	Thorium API calibration coefficient
C_{api}	Potassium API calibration coefficient
CPS	Count rates [counts per second]
C_{sh}	Volumetric concentration of shale
D	Tool collar diameter
D'	Borehole diameter
D_{coeff}	Thermal diffusion coefficient [cm]
eV	Electron volts
f	Gamma calibration factor
GR_{API}	Gamma ray measurement in API units
$K_{\%}$	Potassium concentration on percent
L_d	Diffusion length [cm]
L_m	Migration length [cm]
L_s	Slowing-down length [cm]
m_i	Isotope mass concentration
M_i	Isotope molecular weight

N_{av}	Avogadro’s number
S_i	Isotope pulse height spectra
SO_{max}	Maximum borehole standoff
SO_α	Azimuthally-varying standoff
S_w	Water saturation
$T_{\frac{1}{2}i}$	Isotope half-life
Th_{ppm}	Thorium concentration [ppm]
U_{ppm}	Uranium concentration [ppm]
Z	Atomic number
α	Tool azimuth
ΔD	Effective radial DOI [in]
Δh	Azimuthal depth shift
$\Delta h'$	Azimuthal depth shift for eccentered tool
$\Delta \psi$	Azimuthal aperture
θ	Relative bed dip
θ'	Corrected image relative bed dip
ρ_b	Bulk density
ρ_e	Electron density
ρ_i	Isotope density
Σ	Macroscopic energy cross section [c.u.]
Σ_a	Macroscopic thermal absorption cross section [c.u.]
ϕ	Porosity
ϕ_{sh}	Shale porosity
ϕ_t	Total porosity
ϕ_t'	Model total porosity

Acronyms

^{3}He	Helium-3 isotope
^{40}K	Potassium-40 isotope
^{137}Cs	Caesium-137 isotope
^{232}Th	Thorium-232 isotope
^{238}U	Uranium-238 isotope
DOI	Depth of investigation
D-T	Deuterium-Tritium
EDOI	Effective depth of investigation
EPL	Effective penetration length
EVOI	Effective volume of investigation
FSF	Flux sensitivity function
HA/HZ	High-angle/Horizontal
HI	Hydrogen index
LLDT	Longhorn LWD density tool
LLGT	Longhorn LWD gamma ray tool
LLNT	Longhorn LWD neutron tool
LWD	Logging-while-drilling
MCNP®	Monte Carlo N-Particle code
PEF	Photoelectric factor
SNUPAR©	Schlumberger Nuclear Parameter code
TST	True stratigraphic thickness

References

Badruzzaman, A., Mendoza, A., Stockhausen, E.J., and Reik, B.A., 2007, Density measurement sensitivity to varying borehole angle and tool azimuth in medium to thin beds: Paper J, SPWLA 48th Annual Logging Symposium, June 3-6, Austin, Texas, USA.

Ellis, D.V. and Singer, J.M., 2007, *Well Logging for Earth Scientists*: Springer.

Evans, M., Wraight, P., Marienbach, E., Rhein-Knudsen, E., and Best, D., 1988, Formation porosity measurement while drilling: Paper C, SPWLA 29th Annual Logging Symposium, June 5-8, Houston, Texas, USA.

Flaum, C., Galford, J.E., and Hastings, S., 1987, Enhanced vertical resolution processing of dual detector gamma-gamma density logs: Paper M, SPWLA 28th Annual Logging Symposium, June 29-July 2, Houston, Texas, USA.

Galford, J.E., Flaum, C., Gilchrist, W.A., and Duckett, S.W., 1986, Enhanced resolution processing of compensated neutron logs: SPE 15441, SPE Annual Technical Conference and Exhibition, October 5-8, New Orleans, Louisiana, USA.

Guo, P., Mendoza, A., and Yin, H., 2008, Impact of density tool depth of investigation on dip determination in high angle and horizontal wells, Paper CCCC, SPWLA 49th Annual Logging Symposium, May 25-28, Edinburg, Scotland.

Heidari, Z., Torres-Verdín, C., Mendoza, A., Ijasan, O., and Voss, B., 2009, Rapid, interactive assessment of petrophysical and geometrical effects on density and neutron logs acquired in vertical and deviated wells: SPE 124879, SPE Annual Technical Conference and Exhibition, October 4-7, New Orleans, Louisiana, USA.

McKeon, D.C., and Scott, H.D., 1989, SNUPAR – A nuclear parameter code for nuclear geophysics applications: IEEE Transactions on Nuclear Geoscience, vol. 36, no. 1, February, pp. 1215-1219.

Mendoza, A., Ellis, D.V., Rasmus, J.C., 2006, Why the LWD and wireline gamma ray measurements may read different values in the same well: SPE 101718, 1st International Oil Conference and Exhibition, August 31-September 2, Cancun, Mexico.

Mendoza, A., Torres-Verdín, C., and Preeg, W.E., 2007, Rapid simulation of borehole nuclear measurements based on spatial flux-scattering functions: Paper O, SPWLA 48th Annual Logging Symposium, June 3-6, Austin, Texas, USA.

Mendoza, A., Torres-Verdín, C., and Preeg, W.E., 2010a, Linear iterative refinement method for the rapid simulation of borehole nuclear measurements, Part 1 – Vertical wells: Geophysics, 75(1): E9-E29, January-February.

Mendoza, A., Torres-Verdín, C., and Preeg, W.E., 2010b, Linear iterative refinement method for the rapid simulation of borehole nuclear measurements, Part 2 – High-angle and horizontal wells: Geophysics, 75(2): E79-E90, March-April.

Radke, R.J., Adolph, R.A., Climent, H., Ortenzi, L., and Wijeyesekera, N., 2003, Improved formation evaluation through image-derived density: Paper P, SPWLA 44th Annual Logging Symposium, June 22-25, Galveston, Texas, USA.

Uzoh, E.A., Mendoza, A., Torres-Verdín, C., Preeg, W., Stockhausen, E., and Rasmus, J.C., 2009, Influence of relative dip angle and bed thickness on LWD density images acquired in high-Angle and horizontal wells: Petrophysics, 50(3): 269-293, June.

X-5 Monte Carlo Team, 2005, MCNP – A general Monte Carlo N-particle transport code, Version 5: University of California, Los Alamos National Laboratory, Los Alamos, New Mexico.

Yin, H., Guo, P., and Mendoza, A., 2008, Comparison of processing methods to obtain accurate bulk density compensation and azimuthal density image from dual-detector gamma density measurements in high angle and horizontal wells: Paper M, SPWLA 49th Annual Logging Symposium, May 25-28, Edinburg, Scotland.

Yin, H., Han, X., Xu, L., Guo, W., Shehata, A., and Gardner, R.P., 2006, Field and benchmark studies of LWD nuclear tool response in high angle and horizontal wells: Paper AAA, SPWLA 47th Annual Logging Symposium, June 4-7, Veracruz, Mexico.

VITA

Olabode Ijasan obtained a B.Sc. degree in Electrical and Electronics Engineering from the University of Lagos, Nigeria in 2006 and a M.S.E. degree in Petroleum Engineering from The University of Texas at Austin in 2010. He worked as a formation evaluation intern with ExxonMobil Upstream Research Company and ExxonMobil Exploration Company in the summers of 2009 and 2010 respectively. His professional interests include well-log interpretation, petrophysics, and inverse problems.

Permanent address: 1646 West 6th Street, Apt. A, Austin, Texas 78703.
This thesis was typed by Olabode Ijasan.